Geological Magazine

www.cambridge.org/geo

Original Article

Cite this article: Meng Y-X, Zhang Z-C, Tang J-Z, Zhang H-H, Wang Q, and Ding C (2021) Late Ordovician fore-arc ophiolitic mélange in the southern margin of the Bainaimiao arc: constraints from zircon U–Pb–Hf isotopes and geochemical analyses. *Geological Magazine* **158**: 2042–2062. https://doi.org/10.1017/S0016756821000662

Received: 19 December 2020
Revised: 14 June 2021
Accepted: 15 June 2021
First published online: 2 August 2021

Keywords:
Harihada–Chegendalai ophiolitic mélange; zircon U–Pb dating; Late Ordovician; geochemistry; fore-arc tectonic setting

Author for correspondence:
Zhi-Cheng Zhang,
Email: zczhang@pku.edu.cn

Late Ordovician fore-arc ophiolitic mélange in the southern margin of the Bainaimiao arc: constraints from zircon U–Pb–Hf isotopes and geochemical analyses

Yun-Xi Meng[1,2], Zhi-Cheng Zhang[1,2], Jian-Zhou Tang[1,2], Huai-Hui Zhang[1,2], Qi Wang[1,2] and Cong Ding[1,2]

[1]MOE Key Laboratory of Orogenic Belts and Crustal Evolution, Peking University, Beijing 100871, People's Republic of China and [2]School of Earth and Space Sciences, Peking University, Room 3307, Yifu-2 Building, No. 5 Yiheyuan Road, Haidian District, Beijing 100871, People's Republic of China

Abstract

The Harihada–Chegendalai ophiolitic mélange, which is located between the Bainaimiao arc and the North China Craton, holds significant clues regarding the tectonic setting of the southern margin of the Central Asian Orogenic Belt. The ophiolitic mélange is mainly composed of gabbroic and serpentinized ultramafic rocks. Here, zircon U–Pb dating, *in situ* zircon Hf isotopic, whole-rock geochemical and *in situ* mineral chemical data from the ophiolitic mélange are reported. The zircons in the gabbroic rocks yielded concordia U–Pb ages of 450–448 Ma and exhibited slightly positive $\epsilon_{Hf}(t)$ values (0.87–4.34). The geochemical characteristics of the gabbroic rocks indicate that they were generated from a mantle wedge metasomatized by subduction-derived melts from sediments with continental crust contamination, in a fore-arc tectonic setting. These rocks also experienced the accumulation of plagioclase. The geochemical characteristics of the ultramafic rocks and their Cr-spinels indicate that they may constitute part of residual mantle that has experienced a high degree of partial melting and has interacted with fluids/melts released from the subducted slab in the same fore-arc tectonic setting. The ophiolitic mélange may therefore have formed in this fore-arc tectonic setting, resulting from the northward subduction of the South Bainaimiao Ocean beneath the Bainaimiao arc during Late Ordovician time, prior to the collision between the Bainaimiao arc and the North China Craton during the Silurian to Carboniferous periods.

1. Introduction

The Central Asian Orogenic Belt (CAOB), located between the Siberian Craton to the north and the North China and Tarim cratons to the south, is one of the largest accretionary orogenic belts on Earth. It is thought to have evolved through the accretion of microcontinents, island arcs, fore-arc and back-arc basins, ophiolites, oceanic seamounts and accretionary wedges (Fig. 1a; Xiao *et al.* 2003, 2009; Windley *et al.* 2007; Kröner *et al.* 2010, 2014; Safonova, 2017; Safonova *et al.* 2017; Furnes & Safonova, 2019). The Inner Mongolia–Daxinganling Orogenic Belt (IMDOB) is the eastern extension of the CAOB within China; it is a key to understanding the tectonic evolution of the northern margin of the North China Craton (NCC) (Miao *et al.* 2008; Xu *et al.* 2015).

The Bainaimiao arc belt is located in the southern IMDOB; its tectonic affinity and early Palaeozoic tectonic evolution remain controversial (Xiao *et al.* 2003; Jian *et al.* 2008; Xu *et al.* 2013; Zhang *et al.* 2014). Some researchers regard the Bainaimiao arc as an active continental margin formed by the southward subduction of the Palaeo-Asian Ocean beneath the NCC during early Palaeozoic time (Xiao *et al.* 2003; Xu *et al.* 2013; Li *et al.* 2016; Wu *et al.* 2016). Some researchers consider the Bainaimiao arc to be a Japan-style island arc (Hu *et al.* 1990; Jia *et al.* 2003). Recently, some researchers argued that the Bainaimiao arc is an exotic terrane that collided with the NCC after the northward subduction of the southern Bainaimiao Ocean (Zhang *et al.* 2014; Eizenhöfer & Zhao, 2018; Zhou *et al.* 2018*a*; Ma *et al.* 2019; Liu *et al.* 2020).

Situated between the Bainaimiao arc and the NCC, the Harihada–Chegendalai area is important for understanding the relationship between the Bainaimiao arc and the NCC. Here, this study integrates geochronological, petrological and geochemical analyses of the gabbroic and ultramafic rocks from the Harihada–Chegendalai area in order to (1) constrain the age of the gabbroic rocks, (2) deduce the magma source and magmatic evolution of the gabbroic and ultramafic rocks, and (3) reveal the tectonic setting and the implications for the relationship between the Bainaimiao arc and the NCC.

CAMBRIDGE UNIVERSITY PRESS

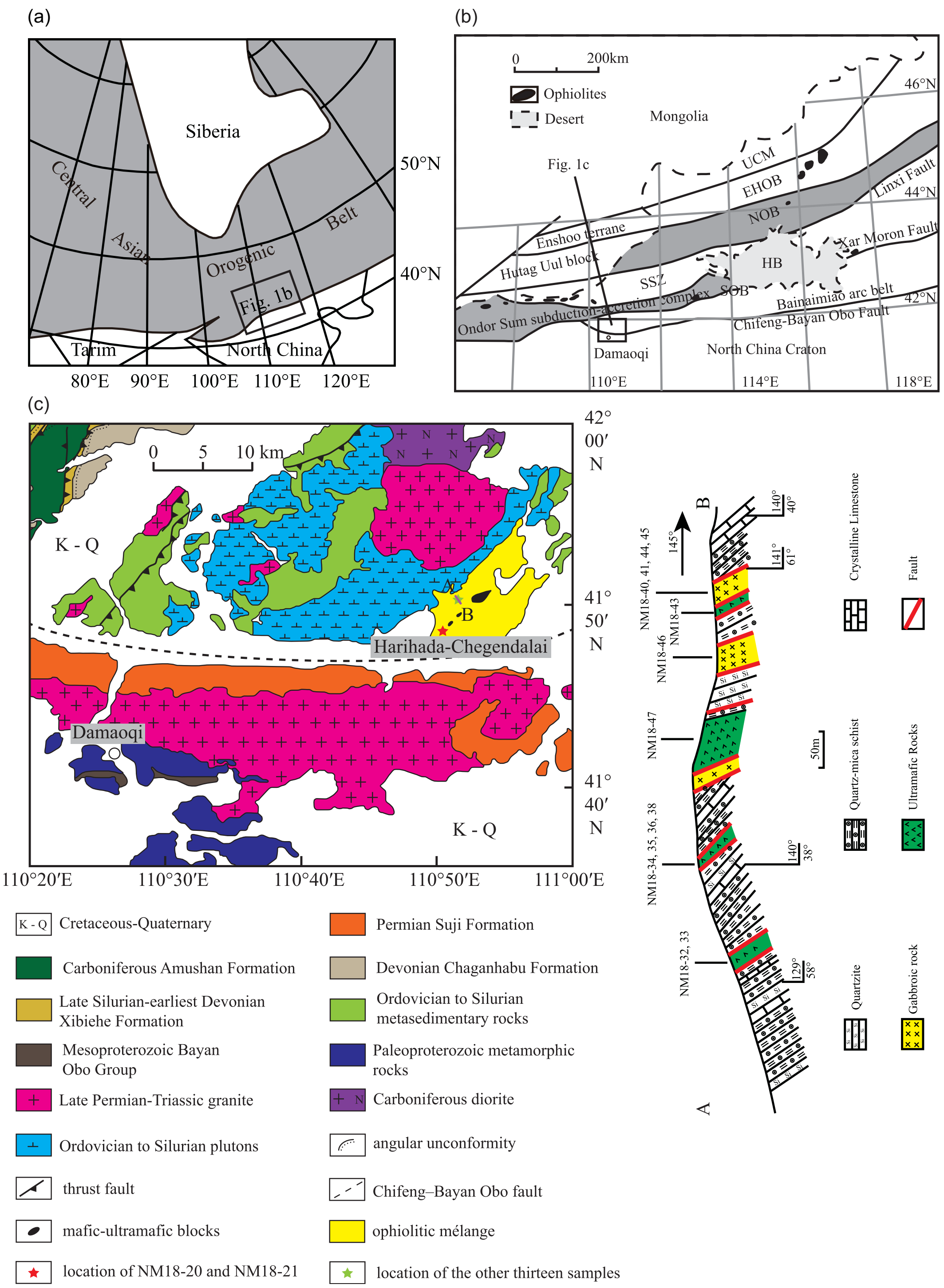

Fig. 1. (Colour online) (a) Simplified tectonic framework of the central-eastern CAOB (modified after Jahn, 2004; Zhang *et al*. 2015). (b) Sketch geological map of the Inner Mongolia – Northern China tract (modified after Chen *et al*. 2015). Abbreviations: SOB – Southern Orogenic Belt; SSZ – Solonker Suture Zone; HB – Hunshandake block; NOB – Northern Orogenic Belt; EHOB – Erenhot–Hegenshan ophiolite belt; UCM – Uliastai continental margin. (c) Geological map of the Damaoqi area (modified after Zhang *et al*. 2014) and geological section of the studied Harihada–Chegendalai ophiolitic mélange.

2. Geological background and sample descriptions

The IMDOB can be divided into the Uliastai continental margin, the Erenhot–Hegenshan ophiolite accretionary belt, the Northern Orogenic Belt, the Solonker Suture Zone and the Southern Orogenic Belt from north to south (Fig. 1b; Xiao *et al.* 2003; Xu *et al.* 2013; Zhang, Z. C. *et al.* 2015, 2017; Ji *et al.* 2018). The Southern Orogenic Belt is mainly composed of the Ondor Sum subduction–accretion complex and the Bainaimiao arc belt from north to south (Xiao *et al.* 2003; Jian *et al.* 2008; Xu *et al.* 2013).

The early to middle Palaeozoic Ondor Sum subduction–accretion complex is mainly composed of turbidites, ophiolitic mélanges, blueschists, plutons, metavolcanics, metasandstones and limestones; it is characterized by S-dipping foliations (Shao,

https://doi.org/10.1017/S0016756821000662 Published online by Cambridge University Press

1989, 1991; Hu *et al.* 1990; Tang, 1992; Jian *et al.* 2008; Xu *et al.* 2013; Li *et al.* 2016; Wu *et al.* 2016; Zhang *et al.* 2018). The Ondor Sum subduction–accretion complex is unconformably overlain by Carboniferous limestones and Permian volcanic-sedimentary rocks (BGMRIM, 1991; Zhou *et al.* 2018*b*). It has been suggested that the Ondor Sum Group was formed by the southward subduction of the Palaeo-Asian Ocean during early Palaeozoic time (Zhou *et al.* 2018*b*). Blueschist-facies quartzite mylonites have exhibited phengite $^{40}Ar–^{39}Ar$ plateau ages of 453.2 ± 1.8 Ma and 449.4 ± 1.8 Ma (De Jong *et al.* 2006), and glaucophanes from a blueschist have yielded $^{39}Ar–^{40}Ar$ ages of 446 ± 15 Ma and 426 ± 15 Ma (Tang & Zhang, 1991). The plutons consist of minor Cambrian–Ordovician granitoids and Permian diorites, quartz diorites and granodiorites (BGMRIM, 1991; Xiao *et al.* 2003; Zhou *et al.* 2018*b*).

The Bainaimiao arc belt is bounded by the Ondor Sum subduction–accretion complex to the north, where the boundary comprises the Xar Moron fault, and is separated from the NCC by the E–W-trending Chifeng–Bayan Obo fault (Xiao *et al.* 2003; Jian *et al.* 2008). The arc belt mainly consists of greenschist-facies–low-amphibolite-facies metasedimentary rocks, volcanic rocks and intermediate-acid intrusive rocks. These arc-related rocks are unconformably overlain by Silurian flysch deposits (Xuniwusu Formation) and Devonian continental molasse or quasi-molasse deposits (Xibiehe Formation; BGMRIM, 1991; Zhang *et al.* 2010; Zhang *et al.* 2014; Zhang, Z. C. *et al.* 2017; Zhou *et al.* 2018*b*; Fig. 1c).

The basement of the NCC is unconformably overlain by Mesoproterozoic rift-related volcanic rocks and lower Palaeozoic passive margin sediments. It consists of highly metamorphosed Archaean and Palaeoproterozoic rocks, including tonalite–trondhjemite–granodiorite rocks, high-K granite and diorite; it is intruded by late Palaeozoic plutons (Xiao *et al.* 2003; Zhao *et al.* 2003; Zhang *et al.* 2004, 2007, 2009, 2014; Zhai & Santosh, 2011; Ma *et al.* 2013, 2014; Wu *et al.* 2016).

The studied area is located at Harihada–Chegendalai in northeastern Damaoqi, north of the Chifeng–Bayan Obo fault. It lies between the NCC and the Bainaimiao arc belt (Fig. 1c). The Harihada–Chegendalai ophiolitic mélange is 15 km long and is composed of ophiolitic peridotites, pyroxene peridotites, gabbros, deep-water cherts and Ordovician–Silurian muscovite leptynites, marbles, quartzites, mica schists and plagioclase amphibole schists (Shao, 1989, 1991; Tang, 1992; Zhang *et al.* 2014).

Six gabbroic samples (NM18-21, NM18-40, NM18-41, NM18-44, NM18-45 and NM18-46) and nine ultramafic samples (NM18-20, NM18-32, NM18-33, NM18-34, NM18-35, NM18-36, NM18-38, NM18-43 and NM18-47) were collected from the Harihada–Chegendalai ophiolitic mélange (Fig. 1c). These gabbroic and ultramafic rocks were in fault contact with each other, and were also in fault contact with mica-quartz schists (Fig. 2a). The gabbroic samples consist of altered plagioclase (30–45 %), hornblende (25–55 %), epidote (5–10 %), chlorite (3–8 %), quartz (2–4 %) and opaque minerals (5–10 %; Fig. 2b). Sample NM18-20 is a harzburgite and contains orthopyroxene (35–40 %), serpentine (55–65 %) and chromite (5–10 %; Fig. 2c). The other ultramafic samples contain serpentine (85–90 %), carbonate minerals (1–10 %), chromite (3–7 %) and spinel (1–3 %; Fig. 2d). Although the degree of serpentinization is high, bastites with orthopyroxene pseudomorphs can be found, and the ultramafic protoliths were deduced to be harzburgites (Fig. 2d).

3. Analytical methods

3.a. Zircon U–Pb dating

Zircon grains were separated from gabbroic rock samples using conventional heavy liquid and magnetic separation techniques. They were manually picked under a binocular microscope. Randomly selected grains were mounted using epoxy resin and polished to expose their interiors. Cathodoluminescence (CL) images were obtained using a FEI Quanta 200F scanning electron microscope (SEM) at the Electron Microscopy Laboratory of Peking University. This permitted observation of the internal structures of the zircon grains. The U–Th–Pb isotope analyses were guided by reflected and transmitted light micrographs and CL images.

Samples NM18-21, NM18-40 and NM18-46 were chosen for zircon U–Pb dating. U–Pb dating and trace-element analyses of zircons were performed synchronously using a laser ablation inductively coupled plasma mass spectrometer (LA-ICP-MS) at the Key Laboratory of Orogenic Belts and Crustal Evolution, Peking University. Zircon 91500 was used as the external standard for age calibration, and the NIST 610 silicate glass was applied as an external standard to calculate concentrations. ^{29}Si was the internal standard. Isotopic ratios, apparent ages and concentrations were calculated using GLITTER software (ver. 4.4.2, Macquarie University). The reported ages were calculated and concordia diagrams were made using Isoplot (version 4.15; Ludwig, 2003). Details of the analytical methods can be found in Tang *et al.* (2014).

3.b. In situ *zircon Hf isotope analyses*

Samples NM18-21, NM18-40 and NM18-46 were chosen for *in situ* zircon Hf isotopic analyses. Zircon Hf isotopic analyses were carried out on a Coherent Geolas HD laser-ablation system, attached to a Nu Plasma II multi-collector inductively coupled plasma mass spectrometer (MC-ICP-MS) at the Key Laboratory of Orogenic Belts and Crustal Evolution, Peking University. Readings were taken from the same zircons used in U–Pb dating, but different sites were used. A beam diameter of 60 μm and a pulse rate of 4 Hz were used during laser ablation with a laser beam energy of 10 J cm^{-2}. Standards 91500, Penglai and Plešovice were used to calibrate the results.

The decay constant of ^{176}Lu is 1.867×10^{-11} $year^{-1}$ (Söderlund *et al.* 2004). The present-day $^{176}Hf/^{177}Hf$ and $^{176}Lu/^{177}Hf$ ratios of chondrite are 0.282785 and 0.0336, respectively (Bouvier *et al.* 2008). Depleted mantle reservoir has a present-day $^{176}Lu/^{177}Hf$ ratio of 0.0384 and a $^{176}Hf/^{177}Hf$ ratio of 0.28325 (Griffin *et al.* 2004). The Hf depleted mantle model ages (T_{DM-Hf}) were calculated by using the measured $^{176}Lu/^{177}Hf$ and $^{176}Hf/^{177}Hf$ ratios of the samples and the present-day $^{176}Lu/^{177}Hf$ and $^{176}Hf/^{177}Hf$ ratios for the depleted mantle.

3.c. Whole-rock geochemical analyses

Whole-rock samples were crushed and milled to ~200 mesh. Major- and trace-element compositions of the samples were obtained from the Key Laboratory of Orogenic Belts and Crustal Evolution, Peking University, Beijing. The range of analytical uncertainty was monitored by analyses of Chinese national standard samples GSR-2 and GSR-3. Major oxides were analysed through X-ray fluorescence using a Jarrell-AshICAP 9000SP spectrometer on fused-glass discs. Loss on ignition (LOI) was determined using the gravimetric method. After acid digestion of

https://doi.org/10.1017/S0016756821000662 Published online by Cambridge University Press

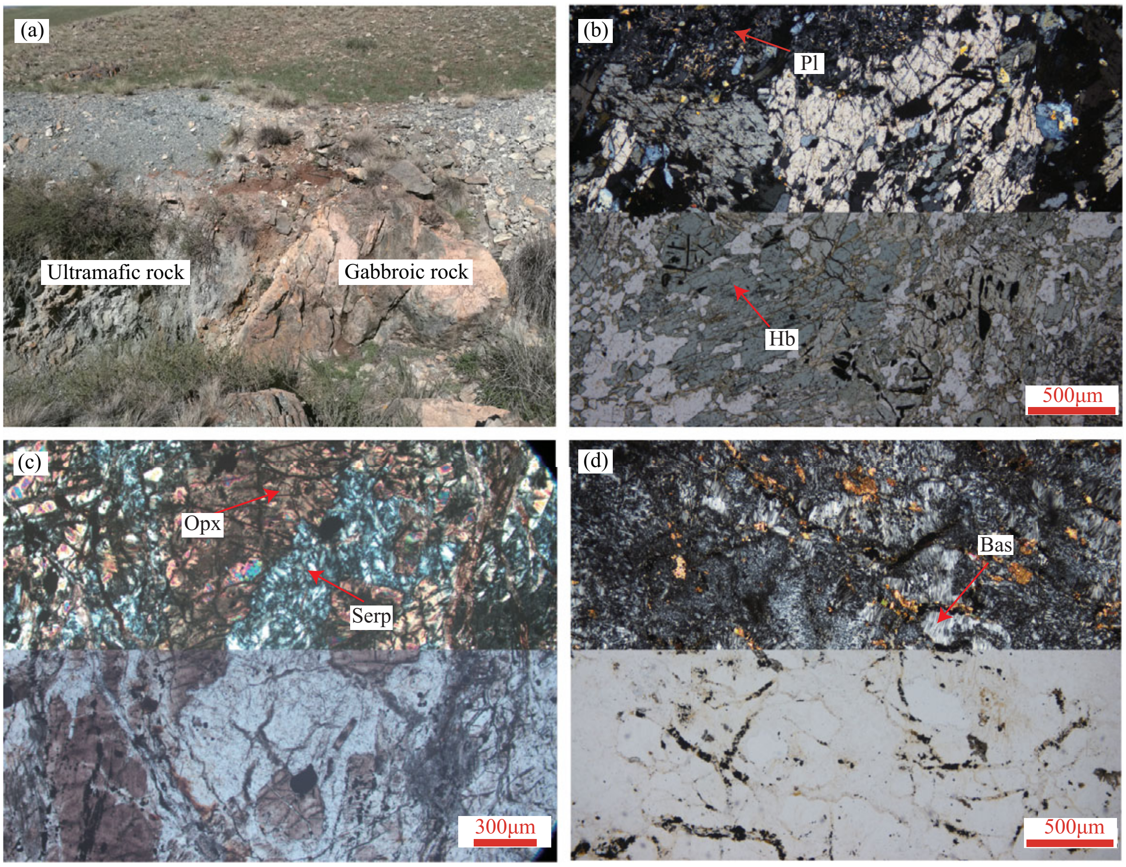

Fig. 2. (Colour online) (a) Contact relationship between gabbroic rocks and ultramafic rocks. (b) Gabbroic rock. (c) Serpentinized harzburgite. (d) Bastites with orthopyroxene pseudomorphs in a serpentinized peridotite. Abbreviations: Pl – plagioclase; Hb – hornblende; Opx – orthopyroxene; Serp – serpentine; Bas – bastite.

whole-rock powders (50 mg) in Teflon bombs, trace elements were analysed by VGAXIOM MC-ICP-MS.

3.d. Mineral chemical analyses

Photos were taken using an environmental SEM under backscattered electron mode; the compositions of minerals were analysed using a JXA-8230 electron microprobe at Peking University. The operating conditions were a 15 kV accelerating voltage and a 10 nA beam current. The beam diameter was set to 1–2 μm. The PRZ correction method was used for standardization. The detailed analytical method can be found in Li *et al.* (2018).

4. Analytical results

4.a. Zircon U–Pb dating

Gabbroic samples (NM18-21, NM18-40 and NM18-46) were dated in this study. The results of LA-ICP-MS zircon U–Pb dating are listed in Table 1. Zircon grains from the three samples were colourless, stubby to elongate, euhedral to subhedral, and 160–320 μm in length with aspect ratios of 1.2–4. CL imaging revealed that they have straight and wide oscillatory growth bands (Fig. 3).

Zircons from sample NM18-21 exhibited varying U (76–218 ppm) and Th (35–113 ppm) concentrations with Th/U ratios of 0.39–0.85. All 30 zircons were concordant or nearly concordant, yielding apparent ^{206}Pb–^{238}U ages of 439–459 Ma, except one spot that exhibited an apparent ^{206}Pb–^{238}U age of 476 Ma; they formed a concordia age of 450 ± 2 Ma (Fig. 4a).

Zircons from sample NM18-40 showed U concentrations from 86 to 276 ppm, Th concentrations from 42 to 213 ppm and Th/U ratios from 0.44 to 0.89. All 30 zircons were concordant or nearly concordant, with apparent ages ranging from 437 to 460 Ma. They yielded a concordia age of 449 ± 1 Ma (Fig. 4b).

Zircons from sample NM18-46 displayed Th contents, U contents and Th/U ratios of 27–136 ppm, 62–293 ppm and 0.34–0.75, respectively. All 30 zircons were concordant or nearly concordant. Their apparent ^{206}Pb–^{238}U ages ranged from 436 to 462 Ma, forming a concordia age of 448 ± 1 Ma (Fig. 4c).

4.b. Zircon Lu–Hf isotopic data

Lu–Hf isotopic data of 30 zircons from samples NM18-21, NM18-40 and NM18-46 are listed in Table 2.

Ten zircon grains from sample NM18-21 yielded $^{176}Hf/^{177}Hf$ ratios of 0.282540–0.282601, $^{176}Lu/^{177}Hf$ ratios of 0.000459–0.001069 and $\epsilon_{Hf}(t)$ values of 1.15–3.27, corresponding to $T_{DM\text{-}Hf}$ ages of 915 to 1002 Ma. Ten zircon grains from sample NM18-40 exhibited $^{176}Hf/^{177}Hf$ ratios of 0.282533–0.282608 and $^{176}Lu/^{177}Hf$ ratios of 0.000482–0.001444. The $\epsilon_{Hf}(t)$ values are positive, ranging from 1.01 to 3.49, corresponding to a $T_{DM\text{-}Hf}$ range of from 901 to 1009 Ma. Ten zircons from sample NM18-46 showed $^{176}Hf/^{177}Hf$ ratios of 0.282531–0.282631 and $^{176}Lu/^{177}Hf$ ratios of 0.000295–0.001076. The $\epsilon_{Hf}(t)$ values for these zircons are 0.87–4.34, corresponding to $T_{DM\text{-}Hf}$ ages of 872 to 1005 Ma. The correlations between the $\epsilon_{Hf}(t)$ values and ages of these zircon grains are presented in Figure 4d.

https://doi.org/10.1017/S0016756821000662 Published online by Cambridge University Press

https://doi.org/10.1017/S0016756821000662 Published online by Cambridge University Press

Table 1. LA-ICP-MS zircon U–Pb data for gabbroic rocks in Harihada–Chegendalai, northeastern Damaoqi

	Th	U		Isotopic ratios						Age (Ma)						
Grain No.	(ppm)	(ppm)	Th/U	$^{207}Pb/^{206}Pb$	1σ	$^{207}Pb/^{235}U$	1σ	$^{206}Pb/^{238}U$	1σ	$^{207}Pb–^{206}Pb$	1σ	$^{207}Pb–^{235}U$	1σ	$^{206}Pb–^{238}U$	1σ	Disc.[a]
NM18-21																
NM18-21-01	63.83	100.25	0.64	0.0560	0.0016	0.5595	0.0156	0.0724	0.0008	453	64	451	10	451	5	0.09
NM18-21-02	91.57	166.69	0.55	0.0574	0.0013	0.5818	0.0126	0.0736	0.0008	506	50	466	8	458	5	1.77
NM18-21-03	35.28	77.70	0.45	0.0552	0.0019	0.5449	0.0182	0.0716	0.0009	422	75	442	12	446	5	−0.85
NM18-21-04	72.88	121.57	0.60	0.0537	0.0015	0.5335	0.0143	0.0721	0.0008	357	62	434	9	449	5	−3.25
NM18-21-05	77.22	133.88	0.58	0.0564	0.0015	0.5481	0.0139	0.0705	0.0008	466	59	444	9	439	5	1.00
NM18-21-06	88.33	140.35	0.63	0.0562	0.0015	0.5463	0.0137	0.0706	0.0008	458	57	443	9	440	5	0.68
NM18-21-07	72.34	117.08	0.62	0.0579	0.0016	0.5737	0.0153	0.0718	0.0008	527	60	460	10	447	5	2.95
NM18-21-08	106.92	202.60	0.53	0.0552	0.0012	0.5429	0.0113	0.0713	0.0007	421	48	440	7	444	4	−0.83
NM18-21-09	54.49	84.81	0.64	0.0554	0.0018	0.5504	0.0176	0.0720	0.0009	429	72	445	12	448	5	−0.69
NM18-21-10	92.44	184.50	0.50	0.0547	0.0013	0.5366	0.0118	0.0711	0.0007	401	51	436	8	443	4	−1.49
NM18-21-11	48.08	124.25	0.39	0.0549	0.0015	0.5526	0.0143	0.0731	0.0008	407	59	447	9	455	5	−1.72
NM18-21-12	73.77	134.93	0.55	0.0533	0.0014	0.5415	0.0138	0.0737	0.0008	342	59	439	9	458	5	−4.10
NM18-21-13	69.46	118.03	0.59	0.0585	0.0017	0.6170	0.0169	0.0766	0.0009	547	62	488	11	476	5	2.61
NM18-21-14	38.64	82.49	0.47	0.0576	0.0019	0.5757	0.0184	0.0725	0.0009	513	72	462	12	452	5	2.26
NM18-21-15	113.18	211.75	0.53	0.0545	0.0012	0.5436	0.0113	0.0724	0.0007	391	49	441	7	450	4	−2.13
NM18-21-16	102.56	120.60	0.85	0.0550	0.0015	0.5597	0.0149	0.0738	0.0008	413	60	451	10	459	5	−1.66
NM18-21-17	99.72	217.95	0.46	0.0536	0.0012	0.5453	0.0113	0.0737	0.0007	356	49	442	7	459	4	−3.64
NM18-21-18	89.58	149.37	0.60	0.0560	0.0014	0.5588	0.0134	0.0723	0.0008	454	55	451	9	450	5	0.13
NM18-21-19	50.58	76.25	0.66	0.0565	0.0020	0.5584	0.0188	0.0717	0.0009	470	76	451	12	447	5	0.87
NM18-21-20	55.62	91.29	0.61	0.0549	0.0020	0.5420	0.0190	0.0716	0.0009	409	79	440	13	446	6	−1.35
NM18-21-21	83.13	151.90	0.55	0.0570	0.0014	0.5628	0.0130	0.0716	0.0008	491	54	453	8	446	5	1.66
NM18-21-22	70.29	119.10	0.59	0.0548	0.0015	0.5453	0.0147	0.0722	0.0008	404	61	442	10	449	5	−1.65
NM18-21-23	71.62	112.94	0.63	0.0572	0.0016	0.5668	0.0155	0.0718	0.0008	500	63	456	10	447	5	1.95
NM18-21-24	63.42	112.34	0.56	0.0549	0.0016	0.5522	0.0155	0.0730	0.0008	408	64	446	10	454	5	−1.67
NM18-21-25	87.63	139.36	0.63	0.0547	0.0015	0.5457	0.0138	0.0723	0.0008	402	58	442	9	450	5	−1.73
NM18-21-26	51.17	84.84	0.60	0.0565	0.0019	0.5654	0.0179	0.0726	0.0009	470	72	455	12	452	5	0.71
NM18-21-27	63.27	98.61	0.64	0.0558	0.0017	0.5585	0.0165	0.0726	0.0009	446	67	451	11	452	5	−0.20
NM18-21-28	46.4	92.26	0.50	0.0556	0.0018	0.5527	0.0173	0.0721	0.0009	436	71	447	11	449	5	−0.47
NM18-21-29	63.82	104.11	0.61	0.0557	0.0017	0.5538	0.0164	0.0721	0.0008	442	67	448	11	449	5	−0.25
NM18-21-30	81.94	139.84	0.59	0.0558	0.0015	0.5512	0.0137	0.0716	0.0008	445	57	446	9	446	5	0.00

(*Continued*)

https://doi.org/10.1017/S0016756821000662 Published online by Cambridge University Press

Table 1. (*Continued*)

NM18-40															
NM18-40-01	69.62	111.86	0.62	0.0550	0.0016	0.5546	0.0152	0.0732	0.0008	411	62	448	10	455	5	−1.60
NM18-40-02	113.95	146.88	0.78	0.0551	0.0014	0.5374	0.0132	0.0707	0.0008	416	56	437	9	441	5	−0.89
NM18-40-03	54.11	86.21	0.63	0.0554	0.0019	0.5412	0.0177	0.0708	0.0009	430	74	439	12	441	5	−0.41
NM18-40-04	140.29	181.18	0.77	0.0555	0.0013	0.5508	0.0123	0.0720	0.0008	431	51	446	8	448	5	−0.62
NM18-40-05	116.31	155.69	0.75	0.0561	0.0014	0.5542	0.0131	0.0717	0.0008	456	54	448	9	446	5	0.36
NM18-40-06	124.63	142.45	0.87	0.0547	0.0015	0.5294	0.0133	0.0702	0.0008	400	59	431	9	437	5	−1.33
NM18-40-07	70.70	131.69	0.54	0.0574	0.0015	0.5787	0.0143	0.0731	0.0008	508	57	464	9	455	5	1.96
NM18-40-08	73.31	117.39	0.62	0.0556	0.0016	0.5491	0.0146	0.0716	0.0008	437	61	444	10	446	5	−0.34
NM18-40-09	133.51	150.28	0.89	0.0562	0.0013	0.5716	0.0127	0.0738	0.0008	459	51	459	8	459	5	−0.02
NM18-40-10	180.16	240.71	0.75	0.0563	0.0012	0.5686	0.0111	0.0732	0.0007	465	46	457	7	456	4	0.35
NM18-40-11	83.07	112.10	0.74	0.0562	0.0017	0.5505	0.0156	0.0711	0.0008	459	65	445	10	443	5	0.63
NM18-40-12	63.47	109.21	0.58	0.0545	0.0016	0.5432	0.0154	0.0723	0.0008	391	65	441	10	450	5	−2.11
NM18-40-13	84.82	146.06	0.58	0.0551	0.0014	0.5553	0.0136	0.0731	0.0008	418	56	448	9	455	5	−1.34
NM18-40-14	86.04	147.74	0.58	0.0565	0.0014	0.5726	0.0138	0.0736	0.0008	470	56	460	9	458	5	0.48
NM18-40-15	161.36	223.24	0.72	0.0569	0.0012	0.5667	0.0114	0.0723	0.0007	486	47	456	7	450	4	1.33
NM18-40-16	108.24	185.00	0.59	0.0557	0.0013	0.5609	0.0120	0.0731	0.0008	439	50	452	8	455	5	−0.59
NM18-40-17	75.58	130.68	0.58	0.0542	0.0015	0.5391	0.0142	0.0722	0.0008	378	61	438	9	449	5	−2.54
NM18-40-18	82.13	137.48	0.60	0.059	0.0015	0.5809	0.0144	0.0715	0.0008	565	56	465	9	445	5	4.49
NM18-40-19	207.30	275.70	0.75	0.0552	0.0011	0.5631	0.0106	0.0740	0.0007	421	44	454	7	460	4	−1.41
NM18-40-20	119.99	149.66	0.80	0.0574	0.0014	0.5762	0.0135	0.0728	0.0008	506	54	462	9	453	5	1.94
NM18-40-21	109.13	201.85	0.54	0.0575	0.0013	0.5749	0.0119	0.0725	0.0008	511	48	461	8	451	4	2.22
NM18-40-22	114.39	135.54	0.84	0.0559	0.0015	0.5526	0.0140	0.0717	0.0008	450	58	447	9	446	5	0.13
NM18-40-23	78.30	153.17	0.51	0.0551	0.0014	0.5495	0.0134	0.0723	0.0008	418	56	445	9	450	5	−1.18
NM18-40-24	41.86	95.15	0.44	0.0576	0.0019	0.5655	0.0177	0.0713	0.0009	513	70	455	11	444	5	2.57
NM18-40-25	144.74	186.79	0.77	0.0554	0.0013	0.5503	0.0120	0.0720	0.0008	429	50	445	8	448	4	−0.69
NM18-40-26	154.69	181.44	0.85	0.0549	0.0013	0.5429	0.0122	0.0717	0.0008	409	52	440	8	446	5	−1.34
NM18-40-27	164.84	220.80	0.75	0.0561	0.0012	0.5583	0.0116	0.0722	0.0007	457	48	450	8	449	4	0.29
NM18-40-28	137.95	170.38	0.81	0.0588	0.0015	0.5828	0.0141	0.0719	0.0008	560	55	466	9	448	5	4.18
NM18-40-29	105.34	141.26	0.75	0.0545	0.0015	0.5356	0.0136	0.0713	0.0008	391	59	436	9	444	5	−1.91
NM18-40-30	212.60	273.39	0.78	0.0561	0.0012	0.5584	0.0109	0.0722	0.0007	456	46	451	7	449	4	0.24
NM18-46															
NM18-46-01	63.13	109.28	0.58	0.0562	0.0016	0.5746	0.0158	0.0742	0.0009	458	63	461	10	462	5	−0.13

(*Continued*)

Table 1. (*Continued*)

Grain No.	Th (ppm)	U (ppm)	Th/U	Isotopic ratios						Age (Ma)						Disc.[a]
				$^{207}Pb/^{206}Pb$	1σ	$^{207}Pb/^{235}U$	1σ	$^{206}Pb/^{238}U$	1σ	$^{207}Pb–^{206}Pb$	1σ	$^{207}Pb–^{235}U$	1σ	$^{206}Pb–^{238}U$	1σ	
NM18-46-02	97.10	212.22	0.46	0.0562	0.0013	0.5653	0.0125	0.0730	0.0008	459	51	455	8	454	5	0.15
NM18-46-03	118.12	292.50	0.40	0.0554	0.0012	0.5470	0.011	0.0716	0.0007	429	47	443	7	446	4	−0.63
NM18-46-04	87.12	130.42	0.67	0.0574	0.0016	0.5595	0.0151	0.0707	0.0008	506	62	451	10	441	5	2.41
NM18-46-05	41.40	71.98	0.58	0.0562	0.0022	0.5456	0.0202	0.0705	0.0009	459	84	442	13	439	6	0.75
NM18-46-06	46.44	111.25	0.42	0.0534	0.0017	0.5258	0.0157	0.0715	0.0009	344	69	429	10	445	5	−3.62
NM18-46-07	56.17	150.57	0.37	0.0572	0.0015	0.5630	0.0142	0.0715	0.0008	497	58	454	9	445	5	1.91
NM18-46-08	60.02	133.13	0.45	0.0557	0.0016	0.5507	0.0148	0.0717	0.0008	442	61	445	10	446	5	−0.18
NM18-46-09	72.70	130.21	0.56	0.0524	0.0015	0.5228	0.0147	0.0724	0.0009	301	66	427	10	451	5	−5.30
NM18-46-10	56.63	107.09	0.53	0.0571	0.0018	0.5712	0.0168	0.0726	0.0009	495	67	459	11	452	5	1.59
NM18-46-11	64.98	150.19	0.43	0.0566	0.0015	0.5597	0.0143	0.0718	0.0008	474	59	451	9	447	5	1.01
NM18-46-12	55.32	94.76	0.58	0.0567	0.0018	0.5704	0.0171	0.0730	0.0009	479	69	458	11	454	5	0.90
NM18-46-13	45.81	84.70	0.54	0.0525	0.0019	0.5203	0.0178	0.0720	0.0009	305	79	425	12	448	6	−5.04
NM18-46-14	71.44	130.69	0.55	0.0556	0.0016	0.5572	0.0151	0.0728	0.0008	435	62	450	10	453	5	−0.68
NM18-46-15	70.47	137.47	0.51	0.0552	0.0016	0.5483	0.0146	0.0721	0.0008	419	61	444	10	449	5	-1.07
NM18-46-16	59.78	174.24	0.34	0.0575	0.0015	0.5584	0.0136	0.0705	0.0008	510	56	451	9	439	5	2.64
NM18-46-17	38.53	73.50	0.52	0.0528	0.0021	0.5184	0.0196	0.0712	0.0010	320	86	424	13	444	6	−4.40
NM18-46-18	74.01	163.10	0.45	0.0539	0.0014	0.5444	0.0136	0.0733	0.0008	367	58	441	9	456	5	−3.18
NM18-46-19	40.14	85.90	0.47	0.0539	0.0019	0.5343	0.0183	0.0720	0.0009	365	78	435	12	448	6	−2.99
NM18-46-20	59.69	127.83	0.47	0.0554	0.0016	0.5347	0.0151	0.0700	0.0008	429	64	435	10	436	5	−0.25
NM18-46-21	33.25	71.85	0.46	0.0548	0.0022	0.5443	0.0207	0.0721	0.0010	402	85	441	14	449	6	−1.72
NM18-46-22	112.07	160.32	0.70	0.0573	0.0015	0.5570	0.0141	0.0706	0.0008	501	58	450	9	440	5	2.27
NM18-46-23	26.86	61.61	0.44	0.0532	0.0023	0.5372	0.0223	0.0733	0.0010	337	94	437	15	456	6	−4.26
NM18-46-24	136.45	186.55	0.73	0.0550	0.0014	0.5413	0.0131	0.0715	0.0008	411	56	439	9	445	5	−1.26
NM18-46-25	83.14	116.70	0.71	0.0540	0.0017	0.5252	0.0156	0.0706	0.0009	371	68	429	10	440	5	−2.48
NM18-46-26	60.15	103.24	0.58	0.0569	0.0018	0.5711	0.0170	0.0728	0.0009	488	68	459	11	453	5	1.28
NM18-46-27	77.41	148.01	0.52	0.0543	0.0015	0.5490	0.0145	0.0734	0.0009	384	61	444	10	456	5	−2.63
NM18-46-28	41.07	75.44	0.54	0.0558	0.0020	0.5626	0.0194	0.0732	0.0010	444	78	453	13	455	6	−0.42
NM18-46-29	89.88	211.02	0.43	0.0564	0.0014	0.5526	0.0132	0.0711	0.0008	469	56	447	9	443	5	0.95
NM18-46-30	67.54	90.08	0.75	0.0590	0.0023	0.5833	0.0222	0.0717	0.0011	568	84	467	14	446	6	4.53

[a]Disc. = (($^{207}Pb–^{235}U$ age)/($^{206}Pb–^{238}U$ age) − 1) × 100.

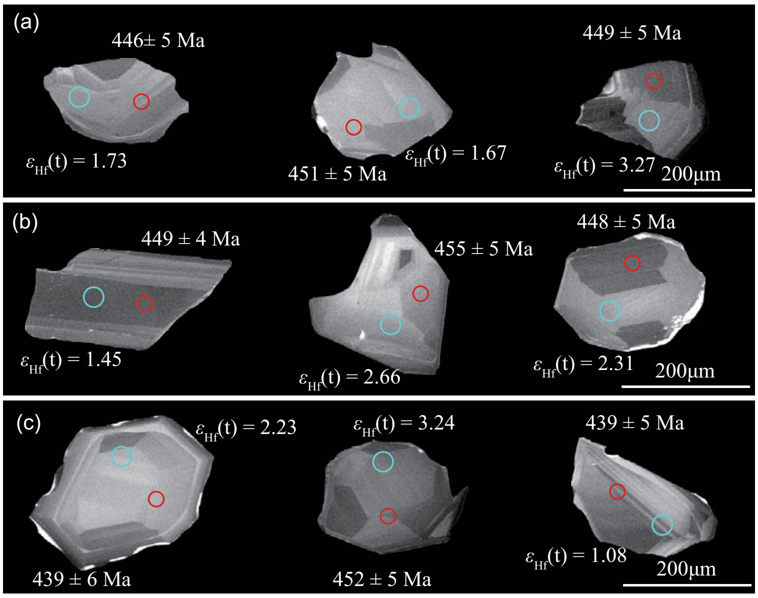

Fig. 3. (Colour online) Cathodoluminescence images of representative zircon grains from (a) sample NM18-21, (b) sample NM18-40, and (c) sample NM18-46. Red and blue circles represent U–Pb and Lu–Hf analysed spots, respectively.

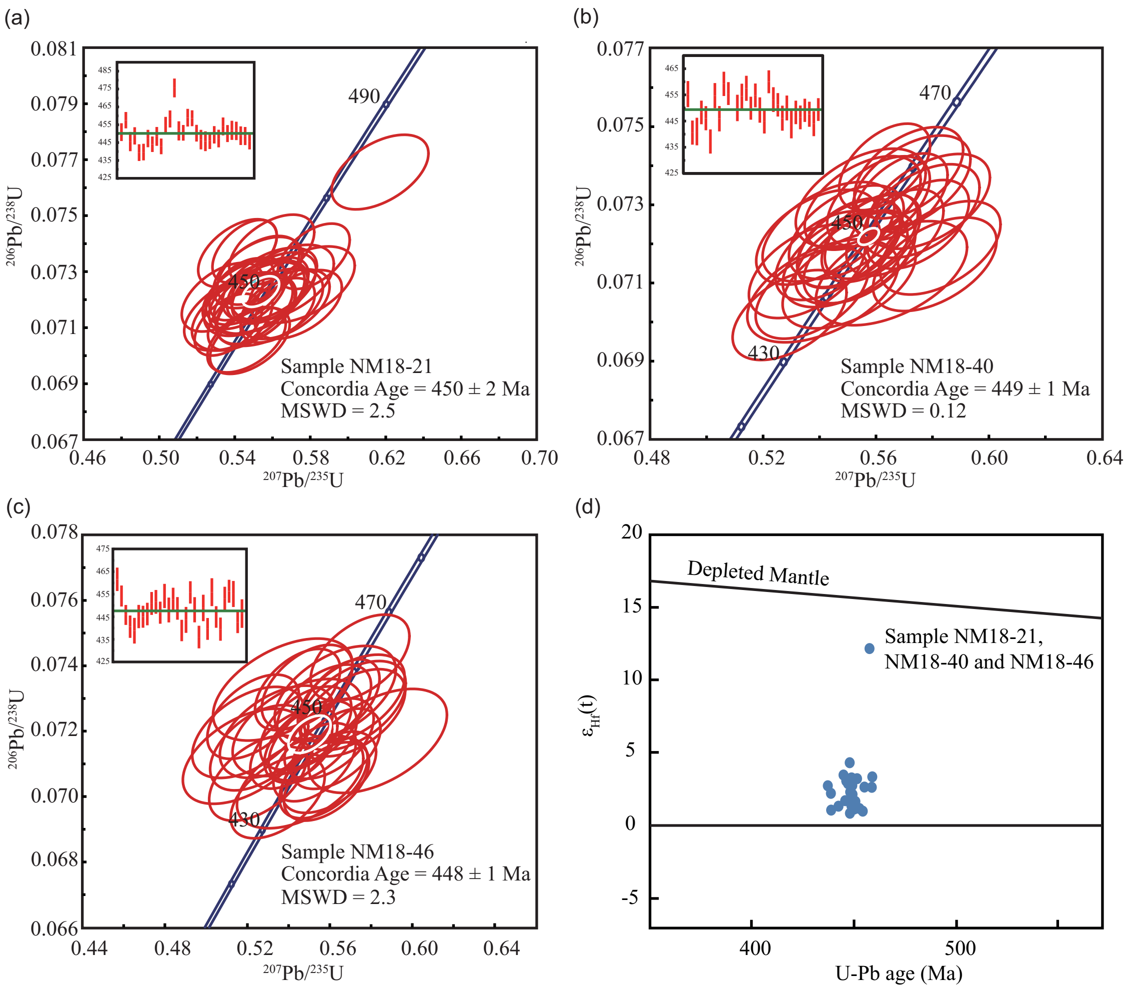

Fig. 4. (Colour online) LA-ICP-MS zircon U–Pb concordia diagrams and weighted average ages of (a) sample NM18-21, (b) sample NM18-40, and (c) sample NM18-46 (the white circles represent the concordia ages). (d) Correlations between $\epsilon_{Hf}(t)$ values and ages of zircon grains of samples NM18-21, NM18-40 and NM18-46.

https://doi.org/10.1017/S0016756821000662 Published online by Cambridge University Press

Table 2. Lu–Hf isotopic data for gabbroic rocks in Harihada–Chegendalai, northeastern Damaoqi

Spot No.	t (Ma)	$^{176}Yb/^{177}Hf$	$^{176}Lu/^{177}Hf$	$^{176}Hf/^{177}Hf$	$2\sigma_m$	$\epsilon_{Hf}(0)$	$\epsilon_{Hf}(t)$	2σ	$T_{(DM-Hf)}$ (Ma)	$f_{Lu/Hf}$
Sample NM18-21										
18-21-01	451	0.025610	0.000678	0.282554	0.000052	−8.17	1.67	1.84	979	−0.98
18-21-04	449	0.030950	0.000740	0.282601	0.000050	−6.51	3.27	1.77	915	−0.98
18-21-07	447	0.046760	0.001069	0.282594	0.000058	−6.75	2.89	2.05	933	−0.97
18-21-16	459	0.023451	0.000552	0.282575	0.000058	−7.43	2.63	2.05	947	−0.98
18-21-18	450	0.037700	0.000843	0.282541	0.000051	−8.63	1.15	1.81	1002	−0.97
18-21-22	449	0.021270	0.000485	0.282584	0.000051	−7.11	2.76	1.81	933	−0.99
18-21-27	452	0.024640	0.000548	0.282540	0.000058	−8.66	1.23	2.05	995	−0.98
18-21-28	449	0.019110	0.000459	0.282545	0.000046	−8.49	1.38	1.63	986	−0.99
18-21-29	449	0.026110	0.000777	0.282599	0.000050	−6.58	3.19	1.77	919	−0.98
18-21-30	446	0.030200	0.000828	0.282560	0.000049	−7.96	1.73	1.73	975	−0.98
Sample NM18-40										
18-40-01	455	0.022850	0.000562	0.282578	0.000063	−7.32	2.66	2.23	943	−0.98
18-40-06	437	0.052050	0.001204	0.282597	0.000063	−6.65	2.74	2.23	932	−0.96
18-40-09	459	0.060040	0.001444	0.282603	0.000066	−6.44	3.36	2.34	930	−0.96
18-40-13	455	0.028280	0.000679	0.282533	0.000058	−8.91	1.01	2.05	1009	−0.98
18-40-17	449	0.034890	0.000854	0.282565	0.000054	−7.78	1.97	1.91	968	−0.97
18-40-18	445	0.022940	0.000563	0.282608	0.000053	−6.26	3.49	1.88	901	−0.98
18-40-25	448	0.029060	0.000718	0.282574	0.000054	−7.46	2.31	1.91	952	−0.98
18-40-26	446	0.047390	0.001119	0.282600	0.000060	−6.54	3.07	2.12	926	−0.97
18-40-27	449	0.043680	0.001058	0.282552	0.000059	−8.24	1.45	2.09	992	−0.97
18-40-30	449	0.018702	0.000482	0.282567	0.000047	−7.71	2.16	1.66	956	−0.99
Sample NM18-46										
18-46-05	439	0.019151	0.000518	0.282576	0.000070	−7.39	2.23	2.48	945	−0.98
18-46-10	452	0.017080	0.000461	0.282596	0.000057	−6.68	3.24	2.02	915	−0.99
18-46-11	447	0.010561	0.000295	0.282596	0.000055	−6.68	3.19	1.95	911	−0.99
18-46-13	448	0.026630	0.000670	0.282631	0.000056	−5.45	4.34	1.98	872	−0.98
18-46-14	453	0.017240	0.000454	0.282537	0.000057	−8.77	1.18	2.02	997	−0.99
18-46-16	439	0.038042	0.001076	0.282548	0.000068	−8.38	1.08	2.41	998	−0.97
18-46-19	448	0.015700	0.000449	0.282531	0.000056	−8.98	0.87	1.98	1005	−0.99
18-46-21	449	0.016660	0.000439	0.282599	0.000063	−6.58	3.29	2.23	911	−0.99
18-46-29	443	0.026330	0.000719	0.282550	0.000060	−8.31	1.34	2.12	986	−0.98
18-46-30	446	0.025770	0.000760	0.282597	0.000074	−6.65	3.07	2.62	921	−0.98

4.c. Major and trace elements

The analytical results of the major and trace elements of 15 samples and standard samples GSR-2 and GSR-3 are listed in Table 3.

4.c.1. Major elements

The gabbroic samples yielded moderate SiO_2 (50.36–55.57 wt %) and K_2O (0.93–1.42 wt %); low TiO_2 (0.73–1.39 wt %); and high Na_2O (3.01–4.35 wt %), Al_2O_3 (16.36–21.11 wt %), CaO (7.69–11.28 wt %), MgO (1.87–5.26 wt %) and total Fe_2O_3 (6.43–8.60 wt %); Mg no. values ranged from 0.36 to 0.56. The major elements of the gabbroic rocks were recalculated on an anhydrous basis before plotting. On the diagram of Zr/TiO_2 versus Nb/Y, the gabbroic rocks mainly plotted in the field of basalt (Fig. 5a). On the K_2O (wt %) versus SiO_2 (wt %) diagram, six gabbroic samples plotted in the medium-K field (Fig. 5b).

The compositions of the ultramafic samples showed ranges of SiO_2 = 36.37–44.20 wt %, Al_2O_3 = 1.36–3.54 wt %, total Fe_2O_3 = 5.29–13.08 wt %, CaO = 0.03–3.34 wt %, MgO = 29.96–34.69 wt %, K_2O = 0.03 wt %, Na_2O = 0.01–0.08 wt % and TiO_2 = 0.001–0.01 wt %. The major elements are recalculated based on anhydrous

https://doi.org/10.1017/S0016756821000662 Published online by Cambridge University Press

https://doi.org/10.1017/S0016756821000662 Published online by Cambridge University Press

Table 3. Major- (wt %) and trace-element (ppm) data for gabbroic and ultramafic rocks in Harihada–Chegendalai, northeastern Damaoqi

Rock Type	Gabbroic rocks						Ultramafic rocks									GSR			
Sample	NM18-21	NM18-40	NM18-41	NM18-44	NM18-45	NM18-46	NM18-20	NM18-32	NM18-33	NM18-34	NM18-35	NM18-36	NM18-38	NM18-43	NM18-47	GSR-2 (m)	GSR-2 (s)	GSR-3 (m)	GSR-3(s)
SiO_2	55.28	50.71	52.11	55.57	51.38	50.36	40.49	39.21	42.31	36.37	38.59	38.92	40.62	44.20	42.14	60.89	60.62	44.68	44.64
Al_2O_3	18.20	19.85	18.22	18.91	16.36	21.11	2.63	3.54	2.75	2.15	2.10	1.50	1.36	2.80	3.48	16.17	16.17	13.80	13.83
Fe_2O_3t	6.60	8.60	8.30	6.43	8.04	6.88	9.46	8.66	5.29	13.08	11.81	11.15	9.05	5.81	9.06	4.87	4.90	13.44	13.40
CaO	8.14	9.14	9.60	7.69	11.28	9.10	0.54	2.30	1.69	3.34	0.51	0.84	1.12	0.03	0.88	5.17	5.20	8.86	8.81
MgO	1.87	3.41	3.29	2.65	5.26	2.33	33.16	32.06	34.24	29.96	32.31	32.63	33.23	34.69	31.49	1.73	1.72	7.66	7.77
K_2O	1.42	1.05	1.04	0.93	1.16	1.16	0.03	0.03	0.03	0.03	0.03	0.03	0.03	0.03	0.03	1.89	1.89	2.32	2.32
Na_2O	4.15	3.01	3.27	4.35	3.16	4.14	0.03	0.08	0.04	0.01	0.03	0.01	0.01	0.08	0.07	3.86	3.86	3.36	3.38
MnO	0.12	0.14	0.12	0.11	0.14	0.11	0.09	0.05	0.05	0.10	0.08	0.08	0.06	0.18	0.12	0.08	0.08	0.17	0.17
TiO_2	1.25	1.20	1.22	0.85	0.73	1.39	0.00	0.00	0.00	0.01	0.00	0.00	0.00	0.00	0.01	0.52	0.52	2.34	2.37
P_2O_5	0.44	0.50	0.51	0.33	0.16	0.57	0.01	0.01	0.01	0.01	0.01	0.01	0.01	0.00	0.01	0.23	0.24	0.95	0.95
LOI	2.34	2.25	2.13	2.02	2.20	2.68	13.20	13.75	13.30	14.69	14.19	14.46	14.12	11.83	12.42	4.44	4.44	2.24	2.24
Total	99.82	99.87	99.83	99.85	99.86	99.83	99.64	99.70	99.71	99.72	99.66	99.63	99.61	99.64	99.70	99.85	99.63	99.82	99.87
Mg no.	0.36	0.44	0.44	0.45	0.56	0.40	0.87	0.88	0.93	0.82	0.84	0.85	0.88	0.92	0.87	0.41	0.41	0.53	0.53
Li	7.79	8.84	8.87	9.07	14.90	9.18	21.80	1.33	1.03	0.84	8.87	9.18	5.48	1.18	1.00	18.78	18.30	10.04	9.50
Be	1.59	1.51	0.74	1.13	1.89	0.95	0.03	0.03	0.05	0.17	0.12	0.02	0.02	0.29	0.06	1.17	1.10	2.69	2.50
P	1578.00	1679.00	1699.00	1166.00	1001.00	1759.00	11.30	44.30	52.10	33.30	71.30	14.10	14.80	34.70	19.50	1062.71	1030.00	4609.79	4130.00
Sc	17.35	22.40	25.80	14.90	65.40	17.90	4.99	6.54	5.51	6.38	5.30	4.90	4.48	5.45	9.20	9.12	9.50	16.06	15.20
Ti	8739.00	8205.00	8114.00	5699.00	8893.00	8876.00	60.40	115.00	116.00	186.00	44.30	63.30	49.30	57.40	123.00	3328.17	3090.00	15813.60	14200.00
V	153.00	217.00	171.00	114.00	313.00	131.00	41.70	39.00	30.00	31.00	22.70	23.80	19.80	25.80	54.00	102.01	94.00	200.14	167.00
Mn	1042.00	1086.00	1013.00	829.00	1969.00	854.00	632.00	368.00	370.00	696.00	561.00	576.00	419.00	1373.00	841.00	598.25	604.00	1434.95	1310.00
Co	12.40	20.50	16.70	12.70	42.30	10.70	105.00	82.70	59.50	64.20	106.00	101.00	98.20	76.60	82.70	12.62	13.20	51.35	46.50
Cu	18.90	23.30	27.20	5.69	13.50	5.22	1.29	2.20	2.07	7.87	3.24	1.96	2.94	8.39	24.00	54.95	55.00	52.29	49.00
Ga	23.20	22.10	22.70	21.10	33.20	22.10	0.54	0.66	0.49	1.14	0.25	0.28	0.29	0.73	1.85	18.86	18.10	26.22	24.80
Rb	38.60	34.80	24.60	27.20	55.10	35.10	0.06	0.65	0.17	0.10	0.15	0.05	0.06	0.04	0.05	39.43	38.00	41.60	37.00
Sr	1038.00	1030.00	899.00	1077.00	1406.00	1339.00	13.90	27.30	18.30	34.60	7.82	28.40	14.40	2.15	7.84	821.13	790.00	1194.58	1100.00
Y	17.10	18.60	17.40	12.30	35.30	12.30	0.14	0.35	0.24	0.90	0.06	0.09	0.13	0.54	0.51	8.60	9.30	23.67	22.00
Zr	64.30	78.90	65.60	86.00	135.00	43.10	0.33	1.21	0.84	0.71	0.20	0.49	0.23	0.58	0.68	94.60	99.00	307.23	277.00
Nb	10.20	7.35	5.95	8.55	8.77	7.65	bdl	bdl	0.00	0.34	bdl	0.04	bdl	0.13	0.09	5.71	6.80	75.64	68.00
Cs	2.05	1.81	1.31	1.32	1.55	1.07	0.05	0.04	0.07	0.05	0.04	0.04	0.04	0.01	0.04	1.74	2.30	0.45	0.70
Ba	592.00	592.00	501.00	495.00	611.00	425.00	2.20	16.80	7.55	2.10	7.41	10.20	15.10	1.93	0.75	1054.61	1020.00	551.29	527.00
La	28.80	26.30	24.70	21.10	32.00	22.80	0.02	0.15	0.14	0.63	0.14	0.20	0.16	0.40	0.18	20.85	22.00	55.99	56.00
Ce	58.20	54.00	44.00	42.20	67.60	43.20	0.04	0.25	0.25	1.39	0.30	0.38	0.30	0.94	0.41	40.56	40.00	111.61	105.00

(*Continued*)

Table 3. (*Continued*)

Rock Type	Gabbroic rocks						Ultramafic rocks									GSR			
Sample	NM18-21	NM18-40	NM18-41	NM18-44	NM18-45	NM18-46	NM18-20	NM18-32	NM18-33	NM18-34	NM18-35	NM18-36	NM18-38	NM18-43	NM18-47	GSR-2 (m)	GSR-2 (s)	GSR-3 (m)	GSR-3(s)
Pr	6.62	6.46	5.96	4.57	8.84	5.14	0.01	0.04	bdl	0.17	0.04	0.04	0.04	0.12	0.05	4.60	4.90	12.82	13.20
Nd	26.80	26.80	24.60	17.40	37.90	20.60	0.04	0.20	bdl	0.69	0.13	0.13	0.14	0.52	0.22	17.91	19.00	52.21	54.00
Sm	5.12	5.53	5.02	3.29	8.80	3.96	0.01	0.04	0.04	0.13	0.01	0.02	0.02	0.11	0.06	3.31	3.40	10.41	10.20
Eu	2.00	1.97	1.82	1.51	2.78	2.10	0.00	0.01	0.01	0.06	0.02	0.02	0.02	0.02	0.01	1.05	1.02	3.34	3.20
Gd	4.45	4.86	4.48	2.97	8.07	3.48	0.01	0.05	0.03	0.14	0.01	0.02	0.02	0.11	0.07	2.71	2.70	9.06	8.50
Tb	0.57	0.66	0.60	0.41	1.17	0.44	0.00	0.01	0.01	0.02	0.00	0.00	0.00	0.02	0.01	0.33	0.41	1.13	1.20
Dy	3.23	3.79	3.45	2.44	7.00	2.50	0.02	0.05	0.01	0.15	0.01	0.02	0.03	0.11	0.09	1.77	1.85	5.70	5.60
Ho	0.61	0.71	0.65	0.47	1.34	0.46	0.01	0.01	0.01	0.03	0.00	0.00	0.01	0.02	0.02	0.32	0.34	0.89	0.88
Er	1.69	1.98	1.83	1.37	3.76	1.27	0.02	0.04	0.03	0.10	0.01	0.01	0.02	0.06	0.06	0.84	0.85	2.01	2.00
Tm	0.23	0.27	0.25	0.20	0.52	0.17	0.00	0.01	0.00	0.02	0.00	0.00	0.00	0.01	0.01	0.11	0.15	0.23	0.28
Yb	1.43	1.71	1.58	1.30	3.32	1.06	0.02	0.04	0.03	0.12	0.01	0.01	0.02	0.05	0.07	0.72	0.89	1.23	1.50
Lu	0.22	0.26	0.24	0.21	0.51	0.16	0.00	0.01	0.00	0.02	0.00	0.00	0.00	0.01	0.01	0.11	0.12	0.17	0.19
Hf	1.72	2.20	1.80	2.39	3.87	1.17	0.01	0.03	0.03	0.03	0.01	0.02	0.01	0.01	0.02	2.65	2.90	6.46	6.50
Ta	0.66	0.56	0.46	0.74	0.56	0.48	bdl	bdl	0.00	bdl	bdl	bdl	bdl	bdl	0.07	0.95	0.40	4.09	4.30
Pb	9.41	13.20	8.74	15.10	15.90	13.60	bdl	bdl	bdl	7.29	bdl	bdl	1.02	5.33	4.81	7.39	11.30	10.42	7.00
Th	4.48	4.02	3.65	4.35	6.76	2.00	0.02	0.05	0.03	0.23	0.01	0.03	0.02	0.04	0.02	2.93	2.60	6.00	6.00
U	1.14	0.96	0.83	1.01	1.37	1.06	1.99	0.80	0.33	0.55	0.58	0.84	0.82	0.58	0.15	0.88	0.90	1.34	1.40
δEu	1.28	1.16	1.18	1.48	1.01	1.73	1.10	0.69	0.85	1.27	4.25	3.47	2.40	0.66	0.68	1.07	1.03	1.05	1.05
$(La/Yb)_N$	14.43	10.99	11.21	11.61	6.91	15.43	0.60	2.70	3.60	3.61	14.63	11.88	7.47	5.75	1.84	20.74	17.73	32.60	26.78
∑REE	140.06	135.30	119.32	99.48	183.60	107.45	0.19	0.92	0.56	3.68	0.69	0.85	0.77	2.48	1.27	95.17	97.63	266.80	261.75

bdl – below detection limit; Mg no. = $(MgO/40.3)/(MgO/40.3 + 0.9 * Fe_2O_3/71.84)$; $\delta Eu = Eu_N/(Sm_N * Gd_N)^{1/2}$; GSR-2(m) – measured data for GSR-2; GSR-2(s) – standard data for GSR-2; GSR-3(m) – measured data for GSR-3; GSR-3(s) – standard data for GSR-3.

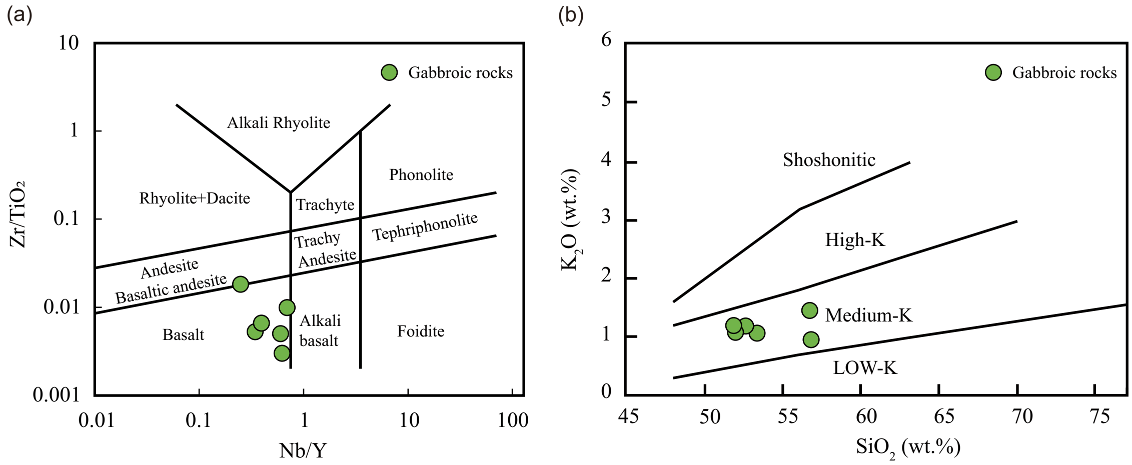

Fig. 5. (Colour online) Geochemical classification plots for the gabbroic rocks: (a) Nb/Y v. Zr/TiO_2 diagram (after Winchester & Floyd, 1977; modified by Pearce, 1996) and (b) SiO_2 v. K_2O diagram (Peccerillo & Taylor, 1976).

ultramafic rocks. The Mg no. values of the ultramafic rocks range from 0.82 to 0.93, with an average of 0.87.

4.c.2. Trace elements

The primitive mantle-normalized trace-element patterns of six gabbroic samples showed enrichment in Rb, Ba, K, Pb and Sr, and depletion in Nb, Ta, Zr, Hf and Ti (Fig. 6a). The total rare earth element (ΣREE) concentrations of six gabbroic samples ranged from 99.48 ppm to 183.60 ppm, with an average of 130.87 ppm. The chondrite-normalized REE patterns showed enriched light rare earth elements (LREEs) and slightly depleted heavy rare earth elements (HREEs): the $(La/Yb)_N$, $(La/Sm)_N$ and $(Gd/Yb)_N$ ratios were 6.91–15.43, 2.35–4.14 and 1.88–2.71, respectively. The gabbroic samples exhibited positive Eu anomalies (δEu = 1.01–1.73, average = 1.31; Fig. 6b).

The primitive mantle-normalized trace-element patterns of the ultramafic samples were characterized by enrichment in fluid-mobile elements (e.g. Ba, U, K, Pb and Sr) and negative Nb, Ta, Zr and Hf anomalies (Fig. 6c). The chondrite-normalized REE diagrams show LREE-enriched profiles. Furthermore, the HREE profiles vary from being depleted to slightly enriched, with $(La/Yb)_N$, $(La/Sm)_N$ and $(Gd/Yb)_N$ ratios of 0.60–14.63, 1.07–6.63 and 0.55–1.72, respectively. The ultramafic samples exhibited both positive and negative Eu anomalies (δEu = 0.66–4.25, average = 1.71; Fig. 6d).

4.d. Spinel chemistry

Fresh Cr-spinel cores and the alteration products of Cr-spinels in sample NM18-32 were analysed by electron probe micro-analyser (EPMA), the compositions were calculated on the basis of 32 oxygens (Jiang & Zhu, 2020) and the results are listed in Table 4. Fresh Cr-spinel cores were enriched in Cr (47.73–55.81 wt % Cr_2O_3), with Cr no. values varying from 0.70 to 0.83 (av. 0.75). They exhibited Mg no. values varying between 0.28 and 0.40, with TiO_2 contents of 0.02–0.21 wt % and Al_2O_3 contents of 7.5–14.66 wt %. The alteration products of the analysed Cr-spinels comprised ferrit-chromite and Cr-magnetite.

5. Discussion

5.a. Late Ordovician ophiolite suite between the Bainaimiao arc belt and the NCC

Previous studies have identified contemporary magmatic events in the Bainaimiao arc belt. Sensitive high-resolution ion microprobe (SHRIMP) zircon U–Pb dating yielded ages of 453.7 ± 3.1 Ma and 457.9 ± 2.6 Ma for a quartz diorite and a dacite in the Tulinkai area, respectively, and a diorite and two quartz diorite adakites yielded ages of 451.5 ± 2.9 Ma, 440.3 ± 2.4 Ma and 446.2 ± 2.2 Ma, respectively (Jian *et al.* 2008). Li *et al.* (2012) reported a molybdenite Re–Os isochron age of 445 ± 3.4 Ma and a weighted ^{206}Pb–^{238}U mean age of 445 ± 6 Ma for a granodiorite porphyry intrusion in the Bainaimiao Cu–Mo deposit. The age of a Bainaimiao meta-volcanic rock was determined to be 449 Ma (Liu *et al.* 2014).

However, magmatic events in the southern margin of Bainaimiao arc belt have not been studied extensively. SHRIMP zircon U–Pb dating yielded ages of 452 ± 3 Ma, 446 ± 2 Ma and 440 ± 2 Ma for a diorite, a quartz diorite and a granodiorite sample in northern Damaoqi, respectively (Zhang & Jian, 2008). LA-ICP-MS zircon U–Pb dating yielded an age of 458 ± 2 Ma for a gabbroic diorite in the Damaoqi area (Zhou *et al.* 2018*b*).

In this study, the zircon LA-ICP-MS U–Pb geochronology of three gabbroic samples yielded crystallization ages of 450 ± 2 Ma, 449 ± 1 Ma and 448 ± 1 Ma, indicating that the ophiolite suite formed during Late Ordovician time.

5.b. Petrogenesis of the gabbroic and ultramafic rocks

5.b.1. Assessment of element mobility

Zr is used as an alteration-independent index for geochemical variations because of its immobility during interactions between igneous rocks and hydrothermal fluids (Gibson *et al.* 1982; Pearce *et al.* 1992; Polat *et al.* 2002). Thus, correlations between trace elements and Zr were used to assess the mobility of trace elements.

Gabbroic samples exhibited LOI values of 2.02–2.68 and exhibited no obvious Ce anomalies ($\delta Ce = Ce_N/Sqrt(La_N \times Pr_N)$) (0.89–1.05). This indicates that the primary chemical signatures of the samples were not significantly affected by alteration and

https://doi.org/10.1017/S0016756821000662 Published online by Cambridge University Press

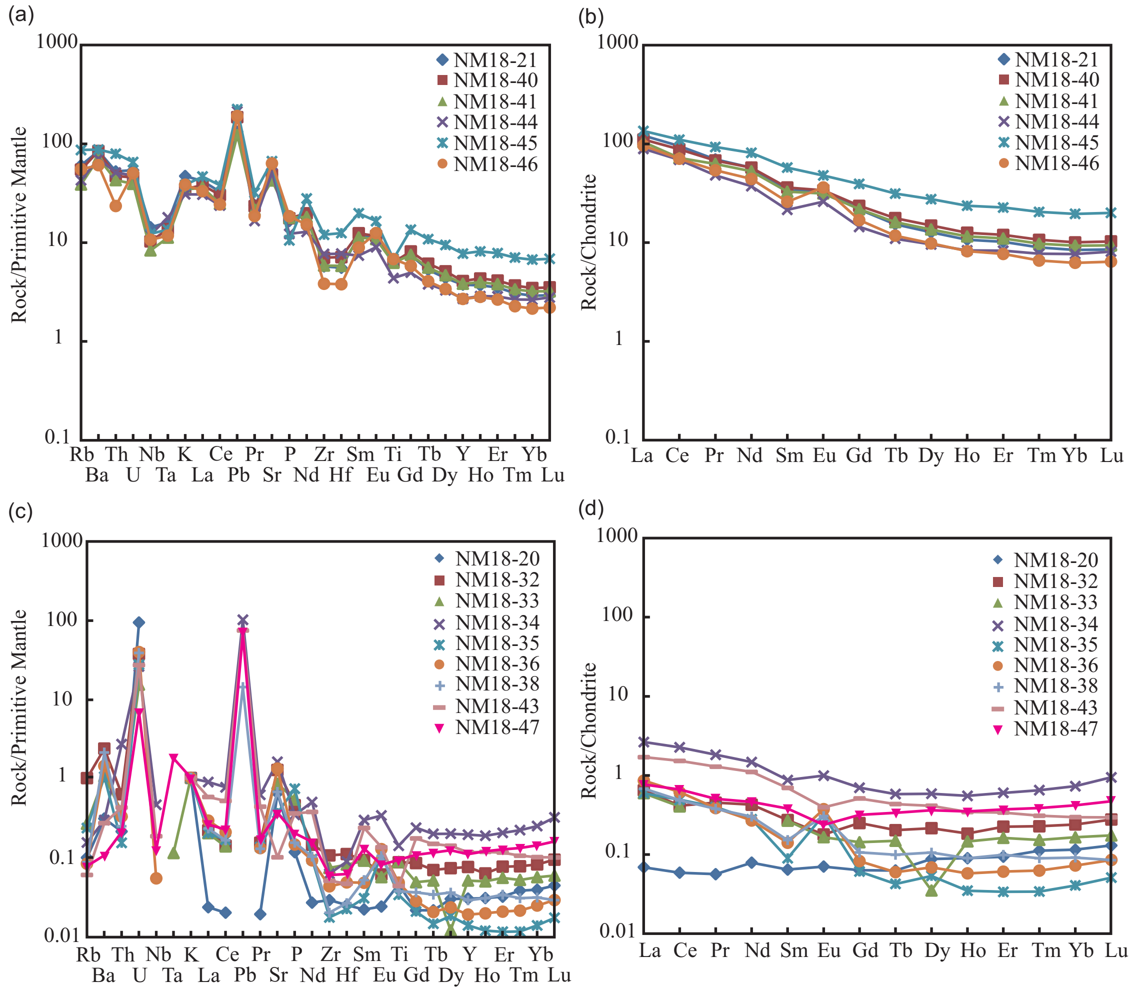

Fig. 6. (Colour online) Primitive mantle-normalized spider patterns and chondrite-normalized REE diagrams for (a, b) gabbroic rocks and (c, d) ultramafic rocks. Primitive mantle- and chondrite-normalized values are from Sun & McDonough (1989).

metamorphism (Polat & Hofmann, 2003). The REEs and high field strength elements (HFSEs) of the gabbroic samples exhibited good correlations with Zr, indicating that these elements were not significantly affected by alteration processes, and thus can be used to discuss petrogenesis. Large-ion lithophile elements (LILEs) also showed correlations with Zr (online Supplementary Material Fig. S1). The results were the same when using correlations between trace elements and TiO_2 to assess the mobility of the trace elements (online Supplementary Material Fig. S1; Furnes *et al.* 2012). The above-mentioned findings are also supported by the nearly parallel patterns of the gabbroic samples on the chondrite-normalized REE and primitive mantle-normalized multi-element diagrams. This indicates that the primary chemical signatures of the gabbroic samples were not significantly obliterated.

Spinels in sample NM18-32 exhibited dark grey cores surrounded by light grey rims (Fig. 7a). The Cr–Al–Fe^{3+} triangular plot can be used to distinguish fresh and altered Cr-spinels (Fig. 7b; Azer *et al.* 2013; Khalil *et al.* 2014). Fresh Cr-spinel cores plotted along the Cr–Al join on this diagram. Ferritchromite and Cr-magnetite rims plotted along the Cr–Fe^{3+} join, indicating that there was a decrease in Al_2O_3 and an increase in Fe_2O_3. The conversion of Cr-spinels to ferritchromite and Cr-magnetite may have resulted from post-magmatic processes, such as serpentinization and ophiolite emplacement, and the cores remain unaffected (Barnes, 2000; Azer *et al.* 2013; Kapsiotis *et al.* 2018).

5.b.2. Petrogenesis of the gabbroic rocks

Zircons from the gabbroic samples exhibited slightly positive $\epsilon_{Hf}(t)$ values (0.87–4.34; Fig. 4d), reflecting the major contribution of the mantle and the limited involvement of the continental crust (Griffin *et al.* 2002). The Nb/La ratios of the gabbroic samples (0.24–0.41) indicate that they were derived from the lithospheric mantle (Smith *et al.* 1999). The Sm/Yb versus Sm diagram suggests that the gabbroic rocks were sourced from the spinel–garnet transitional zone (Fig. 8). It has been suggested that $(Th/Nb)_{PM} > 1$ (Saunders *et al.* 1992) and $(Nb/La)_{PM} < 1$ (Kieffer *et al.* 2004) are two reliable indicators of crustal contamination. The gabbroic rocks exhibited $(Th/Nb)_{PM}$ and $(Nb/La)_{PM}$ values of 2.20–6.47 and 0.23–0.39, respectively, indicating crustal contamination. On the chondrite-normalized diagrams, the gabbroic samples were slightly enriched in LREEs and slightly depleted in HREEs (Fig. 6b). On the primitive mantle-normalized spider diagrams, gabbroic samples were enriched in LILEs (e.g. Rb, Ba, U, K and Sr) and depleted in HFSEs (e.g. Nb, Ta, Zr, Hf and Ti; Fig. 6a).

https://doi.org/10.1017/S0016756821000662 Published online by Cambridge University Press

Table 4. Electron-microprobe analyses of Cr-spinels in sample NM18-32 (by EPMA, in wt %)

Point	1-core	1-rim	2-core	2-rim	3-core	3-rim	4-core	4-rim	5-core	5-rim	6-core	6-rim	7-core	7-rim
MnO	0.59	1.01	0.83	0.84	0.63	1.55	0.55	2.22	0.88	0.53	0.67	1.05	0.70	0.63
Na_2O	bdl	bdl	bdl	bdl	bdl	bdl	bdl	bdl	bdl	bdl	0.03	bdl	bdl	bdl
MgO	6.45	2.34	7.83	2.22	6.34	4.38	7.01	5.21	5.34	1.65	6.24	1.99	5.55	1.77
K_2O	0.01	bdl	bdl	bdl	bdl	bdl	bdl	0.02	bdl	0.01	bdl	bdl	0.03	bdl
Cr_2O_3	52.23	16.18	47.73	13.87	50.44	36.78	51.03	44.47	55.81	9.40	52.56	15.33	53.54	9.97
SiO_2	bdl	0.03	0.06	0.03	0.04	0.03	bdl	bdl	0.04	0.01	0.05	bdl	0.03	0.03
Al_2O_3	12.87	0.10	13.48	0.02	13.38	0.45	14.66	0.97	7.50	bdl	11.59	0.04	9.32	0.03
CaO	0.04	0.01	0.02	0.06	bdl	bdl	bdl	0.03	bdl	bdl	bdl	0.01	0.00	0.05
TiO_2	0.06	0.04	0.19	0.14	0.21	0.24	0.03	0.18	0.05	bdl	0.04	bdl	0.02	0.10
NiO	0.06	0.43	0.12	0.57	0.10	0.37	bdl	0.19	0.06	0.65	bdl	0.48	bdl	0.71
FeO	26.17	74.03	27.79	75.49	27.53	51.61	25.18	43.82	29.19	81.30	27.15	74.02	27.82	78.41
Total	98.48	94.17	98.05	93.24	98.68	95.41	98.47	97.10	98.87	93.55	98.33	92.92	97.01	91.71
Mn	0.14	0.26	0.19	0.22	0.14	0.39	0.12	0.54	0.21	0.14	0.15	0.27	0.17	0.17
Na	0.00	0.00	0.00	0.00	0.00	0.00	0.00	0.00	0.00	0.00	0.02	0.00	0.00	0.00
Mg	2.60	1.05	3.13	1.01	2.55	1.93	2.80	2.25	2.22	0.75	2.54	0.91	2.32	0.82
K	0.00	0.00	0.00	0.00	0.00	0.00	0.00	0.01	0.00	0.00	0.00	0.00	0.01	0.00
Cr	11.18	3.86	10.11	3.34	10.76	8.60	10.80	10.17	12.28	2.26	11.34	3.71	11.88	2.44
Si	0.00	0.01	0.02	0.01	0.01	0.01	0.00	0.00	0.01	0.00	0.01	0.00	0.01	0.01
Al	4.11	0.04	4.26	0.01	4.26	0.16	4.63	0.33	2.46	0.00	3.73	0.01	3.08	0.01
Ca	0.01	0.00	0.01	0.02	0.00	0.00	0.00	0.01	0.00	0.00	0.00	0.00	0.00	0.02
Ti	0.01	0.01	0.04	0.03	0.04	0.05	0.01	0.04	0.01	0.00	0.01	0.00	0.00	0.02
Ni	0.01	0.10	0.03	0.14	0.02	0.09	0.00	0.04	0.01	0.16	0.00	0.12	0.00	0.18
Fe	5.93	18.67	6.23	19.23	6.21	12.77	5.64	10.60	6.80	20.69	6.20	18.97	6.53	20.33
Fe^{2+}	5.24	6.60	4.71	6.66	5.34	5.65	5.08	5.18	5.58	6.95	5.30	6.70	5.50	6.86
Fe^{3+}	0.69	12.07	1.52	12.57	0.88	7.12	0.56	5.42	1.21	13.74	0.90	12.27	1.03	13.48
Mg no.	0.33	0.14	0.40	0.13	0.32	0.25	0.36	0.30	0.28	0.10	0.32	0.12	0.30	0.11
Cr no.	0.73	0.99	0.70	1.00	0.72	0.98	0.70	0.97	0.83	1.00	0.75	1.00	0.79	1.00

bdl – below detection limit; Cr no. = Cr/(Cr + Al) atomic ratio; Mg no. = Mg/(Mg + Fe^{2+}) atomic ratio.

These characteristics indicate a subduction-related origin (Stern, 2002; Pearce & Robinson, 2010; Ma *et al.* 2021). On the Ce/Nb versus Ce diagram, the gabbroic rocks plotted near the field of sediments, indicating the contribution of sediments (Fig. 9a). The gabbroic rocks also exhibited the trends of sediments on the diagrams of Th/Yb versus Ba/La (Fig. 9b), Ba/Th versus Th (Fig. 9c) and U/Th versus Th (Fig. 9d). The positive anomaly in Eu (δEu = 1.01–1.73) indicates the accumulation of plagioclase (Huang & Frey, 2003), which can be corroborated by the observed high Sr and Al_2O_3 contents of the gabbroic rocks. On the diagram of Th/Yb versus Nb/Yb, the gabbroic rocks plotted in the field of continental arcs (Fig. 10). It has been suggested that the Zr content of fore-arc basin basalt (FABB) is lower than that of mid-ocean ridge basalt (MORB) and back-arc basin basalt (BABB; Pearce & Norry, 1979). On the diagram of Zr/Y versus Zr, the gabbroic rocks mainly plotted in the FABB field (Fig. 11a). On the diagram of La/Nb versus Y, the gabbroic rocks mainly plotted in the FABB field or near the FABB field (Fig. 11b). Consequently, the gabbroic rocks could be derived from a mantle wedge in a fore-arc tectonic setting, metasomatized by subduction-derived melts from continental-derived sediments with continental crust contamination, and has experienced the accumulation of plagioclase.

5.b.3. Petrogenesis of the ultramafic rocks

Harzburgites are depleted, refractory residual mantle peridotites that are formed by the partial melting of clinopyroxene-bearing harzburgites and lherzolites (Stern *et al.* 2012). Depleted mantle can be found in fore-arc tectonic settings, because water can reduce the high melting temperature (Azer & Stern, 2007; Khalil *et al.* 2014). In primitive mantle-normalized spider diagrams, the enrichment of fluid-mobile elements results from metasomatism with fluids/melts, and low HFSE contents reflect high degrees of melt extraction (Deschamps *et al.* 2013). Enrichment of LREEs indicates the interaction of peridotites with LREE-enriched melts/fluids, such as boninitic melts and crustal material (Sharma & Wasserburg, 1996; Gruau *et al.* 1998; Parkinson &

https://doi.org/10.1017/S0016756821000662 Published online by Cambridge University Press

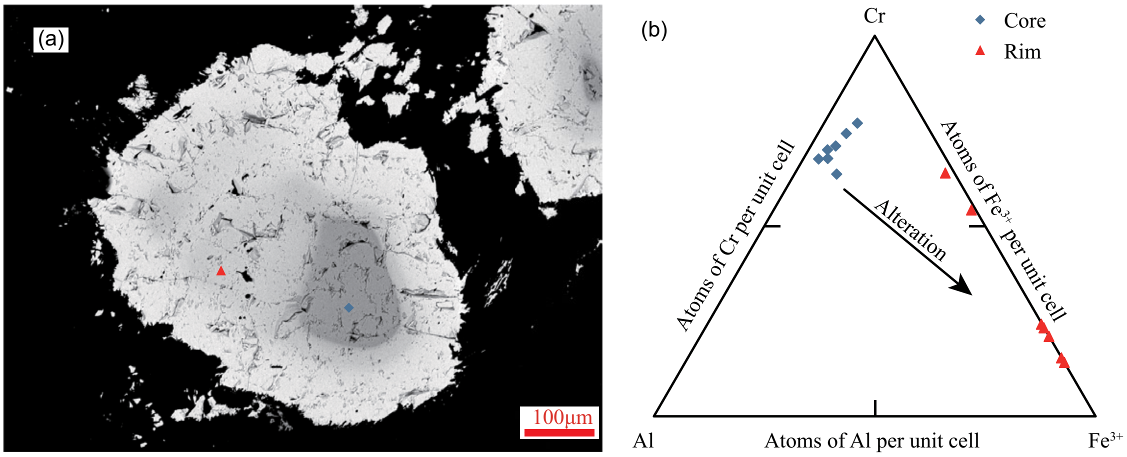

Fig. 7. (Colour online) (a) Spinels with fresh cores and altered rims, and the analysed sites. (b) Cr–Al–Fe^{3+} diagram of cores and rims of Cr-spinels from sample NM18-32.

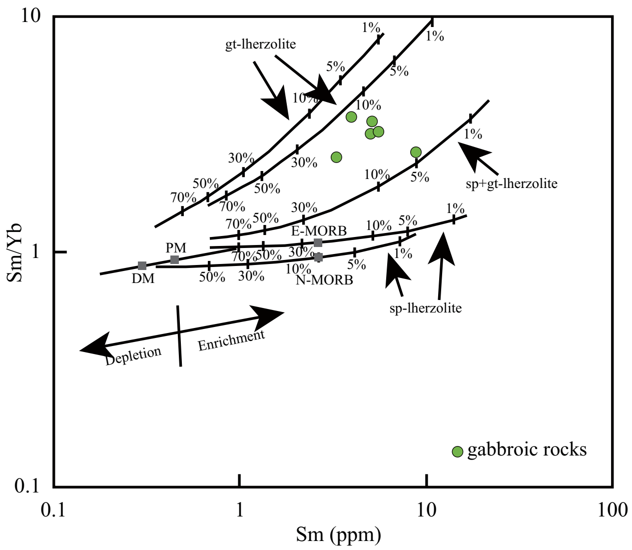

Fig. 8. (Colour online) Sm/Yb v. Sm diagram. Numbers along curves represent the degree of partial melting. The compositions of depleted mantle (DM), primitive mantle (PM), normal mid-ocean ridge basalt (N-MORB), enriched mid-ocean ridge basalt (E-MORB) and melting curves are from Aldanmaz *et al.* (2000).

Pearce, 1998; Zhou *et al.* 2005; Dai *et al.* 2011). The chemical compositions of chromian spinels can indicate different tectonic settings and magma processes (Dick & Bullen, 1984; Barnes & Roeder, 2001; Kamenetsky *et al.* 2001; Arai *et al.* 2011). The spinels from northeastern Damaoqi exhibited high Cr no. values (av. 0.75), indicating that they were formed in the suprasubduction zone tectonic setting, where the melts/fluids released from the subducted slab interacted with the mantle wedge, and the mantle peridotites experienced a high degree of partial melting (Roberts & Neary, 1993; Büchl *et al.* 2004; Zhou *et al.* 2014). The Cr no. values of the spinels were comparable to those of spinels from modern fore-arcs, and distinctly higher than those of spinels from the back-arc basin and mid-ocean ridge (MOR) peridotites (Azer & Stern, 2007). The spinels plotted within the fore-arc peridotite field on the Cr no. versus Mg no. discrimination diagram (Fig. 12a). The contents of TiO_2 in the analysed spinels reflect a magma-producing tectonic setting (Arai, 1992; Arai *et al.* 2011; Arai & Miura, 2016). The TiO_2 versus Cr no. diagram suggests that the spinels may have been generated in fore-arc peridotites, which interacted with the boninitic melt (Fig. 12b). The Al_2O_3 wt % and TiO_2 wt % contents of the spinels indicate a suprasubduction zone origin (Fig. 12c). On the Fe^{2+}/Fe^{3+} atomic ratio versus Al_2O_3 wt % diagram, all of the spinels plotted in the suprasubduction zone peridotite field (Fig. 12d). The characteristics of the spinels and the whole-rock geochemistry of the peridotites jointly indicate that the peridotites may have been residual mantle which has experienced a high degree of partial melting and has interacted with fluids/melts released from a subducted slab in a fore-arc tectonic setting.

5.c. Tectonic implications

Previous studies have suggested that, from north to south, the Ondor Sum subduction–accretion complex, Bainaimiao arc and Xuniwusu Formation form a trench–arc–basin system. This system was thought to have resulted from the southward subduction of the Palaeo-Asian Ocean beneath the NCC (Xiao *et al.* 2003; Zhang, J. F. *et al.* 2017). Located 133 km ENE of the studied area, the Xuniwusu Formation was regarded as a back-arc basin deposit because of its location, flysch sedimentary characteristics and detrital zircon ages (Zhang, J. F. *et al.* 2017).

Both the gabbroic rocks and peridotites were formed in a fore-arc tectonic setting. Furthermore, they crop out together in the schists, so they can be considered as part of the Harihada–Chegendalai ophiolitic mélange. Ophiolites are defined as 'suites of temporally and spatially associated ultramafic, mafic and felsic rocks related to separate melting episodes and processes of magmatic differentiation in particular oceanic environments' (Dilek & Furnes, 2011). They are interpreted to be the remnants of ancient oceanic crust and upper mantle (Dilek & Furnes, 2014). Ophiolites can be classified based on the geochemical fingerprints of their mafic lavas and dykes (Dilek & Furnes, 2011, 2014; Furnes & Dilek, 2017; Furnes *et al.* 2020). As mentioned above, the gabbroic rocks and peridotites analysed in this study are part of a suprasubduction zone ophiolitic mélange; their geochemical characteristics indicate that they were formed in a fore-arc tectonic setting. In recent years, some studies have proposed that there was a South Bainaimiao Ocean between the exotic Bainaimiao arc and the NCC,

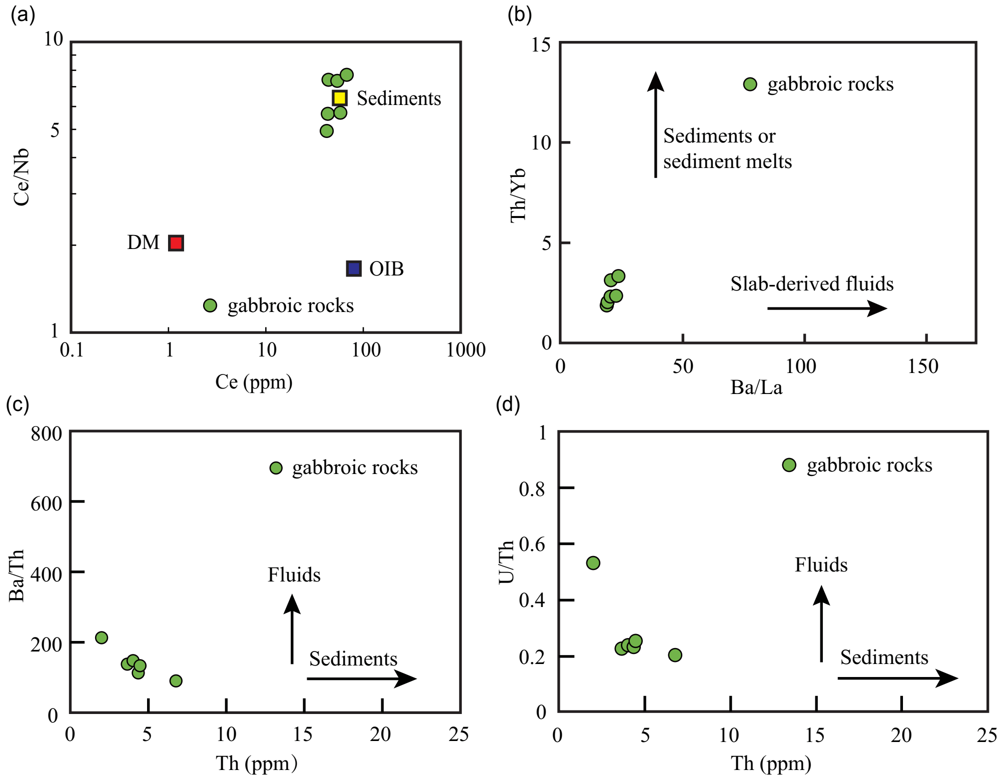

Fig. 9. (Colour online) (a) Ce/Nb–Ce diagram for gabbroic rocks (Ma *et al.* 2021); data for depleted mantle (DM) and ocean-island basalt (OIB) are from Sun & McDonough (1989), and sediment data are from Plank & Langmuir (1998). (b) Th/Yb–Ba/La diagram for gabbroic rocks (Woodhead *et al.* 2001). (c) Ba/Th–Th diagram for gabbroic rocks (Hawkesworth *et al.* 1997). (d) U/Th–Th diagram for gabbroic rocks (Hawkesworth *et al.* 1997).

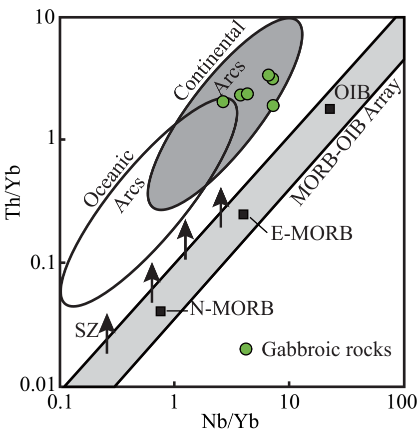

Fig. 10. (Colour online) (a) Th/Yb–Nb/Yb diagram for gabbroic rocks (Pearce, 2014). E-MORB – enriched mid-ocean ridge basalt; N-MORB – normal mid-ocean ridge basalt; OIB – ocean-island basalt; SZ – subduction zone.

and that the northward subduction of the South Bainaimiao Ocean resulted in the collision between the Bainaimiao arc and the NCC during late Silurian to early Carboniferous times (Zhang *et al.* 2014; Eizenhöfer & Zhao, 2018; Zhou *et al.* 2018*a*; Ma *et al.* 2019). The northern NCC was a passive continental margin during early Palaeozoic time, and the Bainaimiao arc has been shown to have a different basement from that of the NCC (Zhang *et al.* 2014). The Xuniwusu Formation can be divided into three sediment cycles; the provenances of the first two sediment cycles comprise solely the Bainaimiao arc (Zhang, J. F. *et al.* 2017). In the last sediment cycle, the Xuniwusu Formation was considered to have received detritus from both the Bainaimiao arc and the NCC, deduced from the detrital zircon ages ranging from Precambrian to Silurian, with the Precambrian detrital zircons considered to have been derived from the NCC (Zhang, J. F. *et al.* 2017). However, the Bainaimiao arc belt also has Precambrian basement, which could have provided detritus to the Xuniwusu Formation. It is also possible that the Xuniwusu Formation received detritus from the NCC because of the shortening of the South Bainaimiao Ocean (Chen *et al.* 2020). The Harihada–Chegendalai ophiolitic mélange may have formed in a fore-arc setting, resulting from the northward subduction of the South Bainaimiao Ocean during Late Ordovician time (Fig. 13).

6. Conclusions

(1) Based on the whole-rock geochemical characteristics, the Late Ordovician (*c.* 448–450 Ma) gabbroic rocks in the Harihada–Chegendalai area (northern Damaoqi) were deduced to have been derived from a mantle wedge that was metasomatized by subduction-derived fluids/melts with continental crust contamination.
(2) According to the whole-rock geochemical characteristics and mineral chemical characteristics, the ultramafic rocks were deduced to comprise part of the depleted residual mantle, which experienced a high degree of partial melting and interacted with fluids/melts released from a subducted slab.
(3) The ultramafic and gabbroic rocks were found to be in fault contact with each other, and to occur together in quartz-mica schists. They comprise part of the Harihada–Chegendalai ophiolitic mélange, which formed in a fore-arc tectonic setting.
(4) Combined with the results of previous studies, the evidence presented here suggests that the South Bainaimiao Ocean

https://doi.org/10.1017/S0016756821000662 Published online by Cambridge University Press

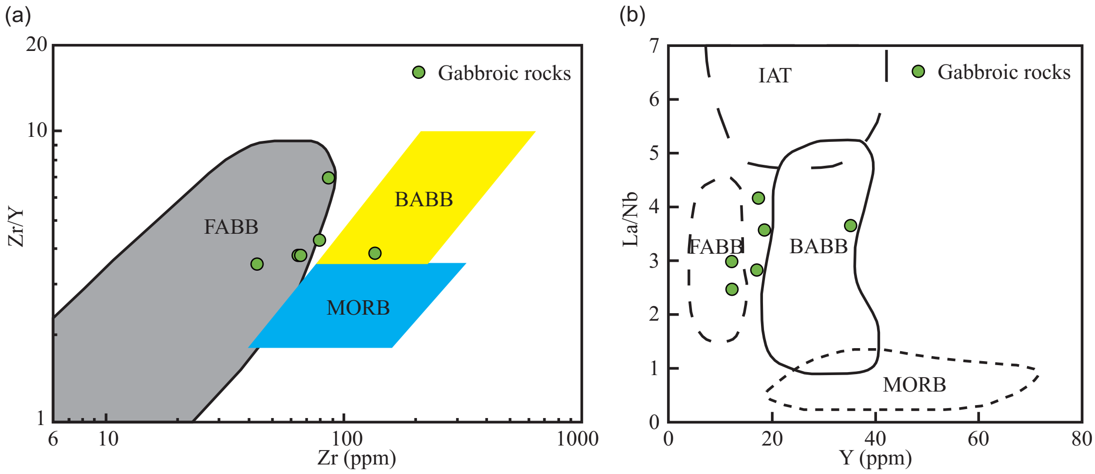

Fig. 11. (Colour online) (a) Zr/Y–Zr diagram for gabbroic rocks (Ma *et al.* 2021). (b) La/Nb–Y diagram for gabbroic rocks (Thanh *et al.* 2012). BABB – back-arc basin basalt; FABB – fore-arc basin basalt; IAT – island arc tholeiite; MORB – mid-ocean ridge basalt.

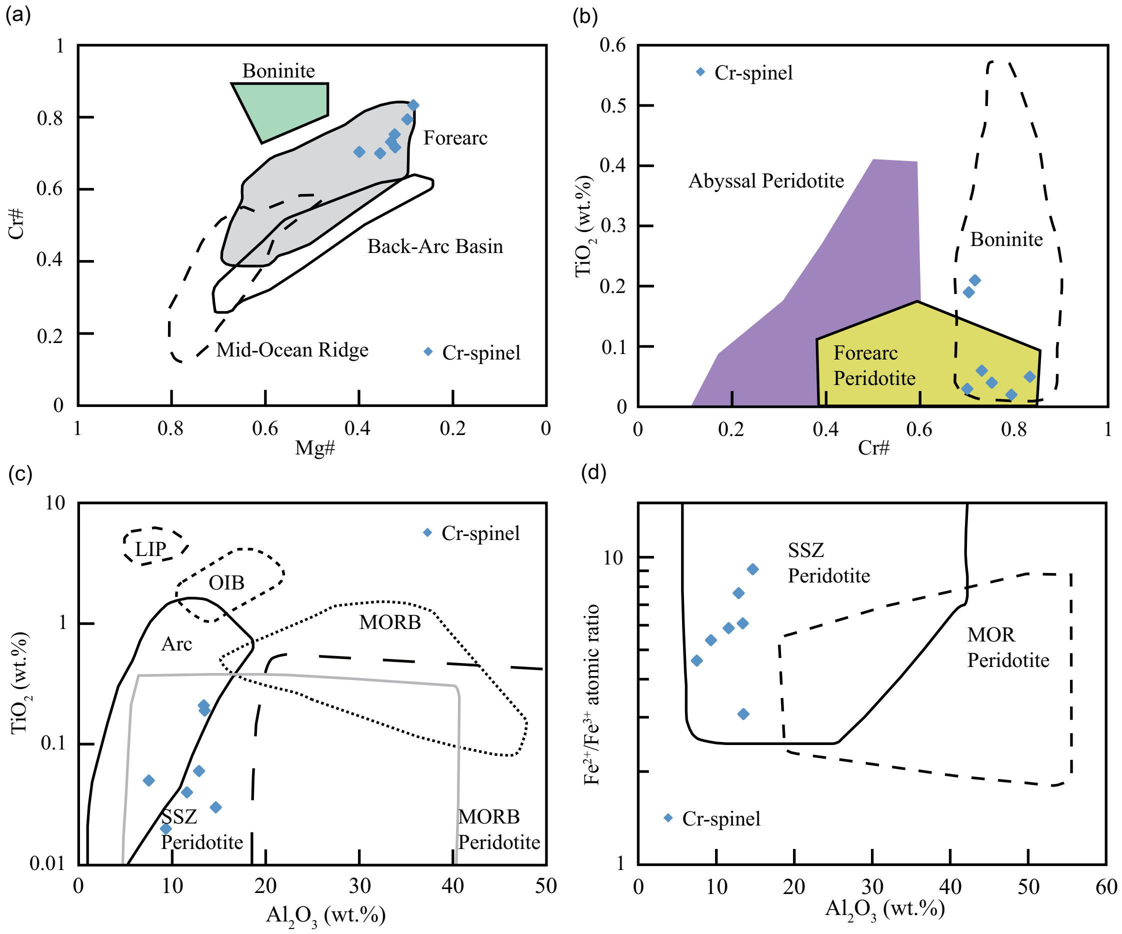

Fig. 12. (Colour online) (a) Cr no.–Mg no. plot for fresh Cr-spinels (after Stern *et al.* 2004). (b) Relationship between Cr no. and TiO_2 content in fresh Cr-spinels (after Tamura & Arai, 2006). (c) TiO_2–Al_2O_3 diagram for fresh Cr-spinels (after Kamenetsky *et al.* 2001). (d) Fe^{2+}/Fe^{3+} atomic ratio–Al_2O_3 wt % plot for fresh Cr-spinels (after Kamenetsky *et al.* 2001). LIP – large igneous province; MOR – mid-ocean ridge; MORB – mid-ocean ridge basalt; OIB – ocean-island basalt; SSZ – suprasubduction zone.

https://doi.org/10.1017/S0016756821000662 Published online by Cambridge University Press

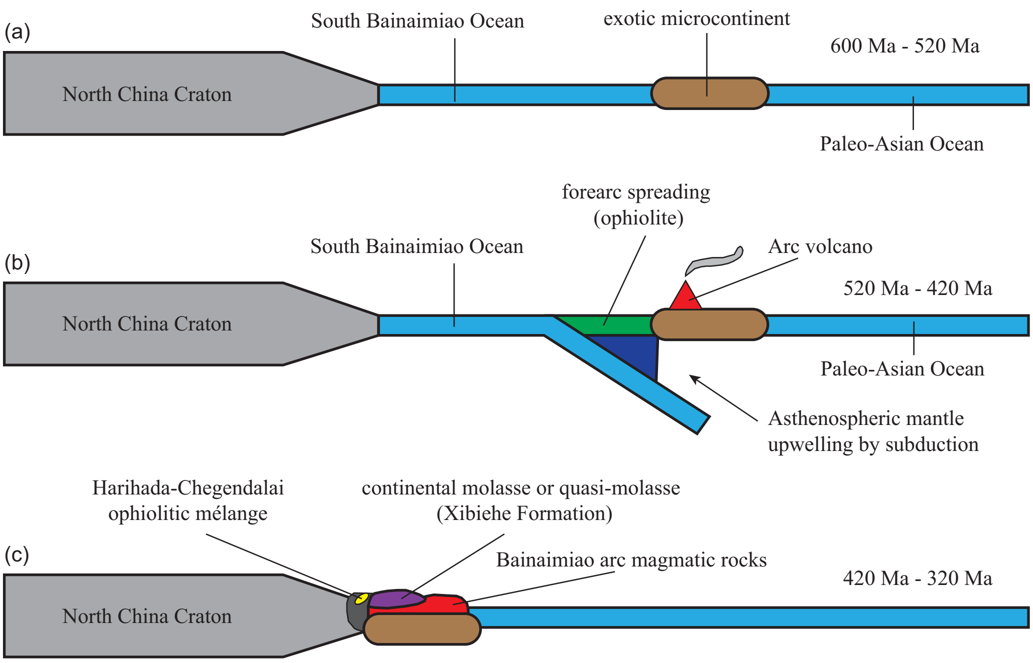

Fig. 13. (Colour online) Tectonic evolution model of the Bainaimiao arc and the north margin of the North China Craton (modified after Zhang *et al.* 2014).

may have subducted northward beneath the Bainaimiao arc during Late Ordovician time, resulting in the formation of the Harihada–Chegendalai fore-arc ophiolitic mélange.

Acknowledgements. We are grateful to Dr Guido Meinhold, Prof. Harald Furnes, Dr Qiangtai Huang and an anonymous reviewer for their precious comments and suggestions. We thank Prof. Shuguang Song and Dr Zeng Lü for their constructive proposals. This study is financially supported by the National Key Research and Development Project of China (grant no. 2017YFC0601302) and the National Key Basic Research Programme of China (grant no. 2013CB429801).

Supplementary material. To view supplementary material for this article, please visit https://doi.org/10.1017/S0016756821000662

References

Aldanmaz E, Pearce JA, Thirlwall M and Mitchell J (2000) Petrogenetic evolution of late Cenozoic, post-collision volcanism in western Anatolia, Turkey. *Journal of Volcanology and Geothermal Research* **102**, 67–95.

Arai S (1992) Chemistry of chromian spinel in volcanic rocks as a potential guide to magma chemistry. *Mineralogical Magazine* **56**, 173–84.

Arai S and Miura M (2016) Formation and modification of chromitites in the mantle. *Lithos* **264**, 277–95.

Arai S, Okamura H, Kadoshima K, Tanaka C, Suzuki S and Ishimaru S (2011) Chemical characteristics of chromian spinel in plutonic rocks: implications for deep magma processes and discrimination of tectonic setting. *Island Arc* **20**, 125–37.

Azer MK, Samuel MD, Ali KA, Gahlan HA, Stern RJ, Ren M and Moussa HE (2013) Neoproterozoic ophiolitic peridotites along the Allaqi-Heiani suture, South Eastern Desert, Egypt. *Mineralogy and Petrology* **107**, 829–48.

Azer MK and Stern RJ (2007) Neoproterozoic (835–720 Ma) serpentinites in the Eastern Desert, Egypt: fragments of forearc mantle. *The Journal of Geology* **115**, 457–72.

Barnes SJ (2000) Chromite in komatiites, II. Modification during greenschist to mid-amphibolite facies metamorphism. *Journal of Petrology* **41**, 387–409.

Barnes SJ and Roeder PL (2001) The range of spinel compositions in terrestrial mafic and ultramafic rocks. *Journal of Petrology* **42**, 2279–302.

BGMRIM (Bureau of Geology and Mineral Resources of Inner Mongolia) (1991) *Regional Geology of Inner Mongolia*. Beijing: Geological Publishing House, 734 pp. (in Chinese).

Bouvier A, Vervoort JD and Patchett PJ (2008) The Lu–Hf and Sm–Nd isotopic composition of CHUR: constraints from unequilibrated chondrites and implications for the bulk composition of terrestrial planets. *Earth and Planetary Science Letters* **273**, 48–57.

Büchl A, Brügmann G and Batanova VG (2004) Formation of podiform chromitite deposits: implications from PGE abundances and Os isotopic compositions of chromites from the Troodos complex, Cyprus. *Chemical Geology* **208**, 217–32.

Chen C, Zhang ZC, Li K, Chen Y, Tang WH and Li JF (2015) Geochronology, geochemistry, and its geological significance of the Damaoqi Permian volcanic sequences on the northern margin of the North China Block. *Journal of Asian Earth Sciences* **97**, 307–19.

Chen Y, Zhang ZC, Qian XY, Li JF, Ji ZJ and Wu TR (2020) Early to mid-Paleozoic magmatic and sedimentary records in the Bainaimiao Arc: an advancing subduction-induced terrane accretion along the northern margin of the North China Craton. *Gondwana Research* **79**, 263–82.

Dai JG, Wang CS, Hébert R, Santosh M, Li YL and Xu JY (2011) Petrology and geochemistry of peridotites in the Zhongba ophiolite, Yarlung Zangbo Suture Zone: implications for the Early Cretaceous intra-oceanic subduction zone within the Neo-Tethys. *Chemical Geology* **288**, 133–48.

De Jong K, Xiao WJ, Windley BF, Masago H and Lo CH (2006) Ordovician ^{40}Ar–^{39}Ar phengite ages from the blueschist-facies Ondor Sum subduction–accretion complex (Inner Mongolia) and implications for the Early Paleozoic history of continental blocks in China and adjacent areas. *American Journal of Science* **306**, 799–845.

Deschamps F, Godard M, Guillot S and Hattori K (2013) Geochemistry of subduction zone serpentinites: a review. *Lithos* **178**, 96–127.

Dick HJB and Bullen T (1984) Chromian spinel as a petrogenetic indicator in abyssal and alpine type peridotites and spatially associated lavas. *Contributions to Mineralogy and Petrology* **86**, 54–76.

Dilek Y and Furnes H (2011) Ophiolite genesis and global tectonics: geochemical and tectonic fingerprinting of ancient oceanic lithosphere. *Geological Society of America Bulletin* **123**, 387–411.

Dilek Y and Furnes H (2014) Ophiolites and their origins. *Elements* **10**, 93–100.

Eizenhöfer PR and Zhao GC (2018) Solonker Suture in East Asia and its bearing on the final closure of the eastern segment of the Palaeo-Asian Ocean. *Earth-Science Reviews* **186**, 153–72.

Furnes H and Dilek Y (2017) Geochemical characterization and petrogenesis of intermediate to silicic rocks in ophiolites: a global synthesis. *Earth-Science Reviews* **166**, 1–37.

Furnes H, Dilek Y, Zhao G, Safonova I and Santosh M (2020) Geochemical characterization of ophiolites in the Alpine-Himalayan Orogenic Belt: magmatically and tectonically diverse evolution of the Mesozoic Neotethyan oceanic crust. *Earth-Science Reviews* **208**, 103258. doi: 10.1016/j.earscirev.2020.103258.

Furnes H, Robins B and De Wit MJ (2012) Geochemistry and petrology of lavas in the upper Onverwacht suit, Barberton mountain land, South Africa. *South African Journal of Geology* **115**, 171–210.

Furnes H and Safonova I (2019) Ophiolites of the Central Asian Orogenic Belt: geochemical and petrological characterization and tectonic settings. *Geoscience Frontiers* **10**, 1255–84.

Gibson SA, Kirkpatrick RJ, Emmermann R, Schmincke PH, Pritchard G, Okay PJ, Thorpe RS and Marriner GF (1982) The trace element composition of lavas and dykes from a 3 km vertical section through a lava pile in Eastern Iceland. *Journal of Geophysical Research* **87**, 6532–46.

Griffin WL, Belousova EA, Shee SR, Pearson NJ and O'Reilly SY (2004) Archean crustal evolution in the northern Yilgarn Craton: U–Pb and Hf-isotope evidence from detrital zircons. *Precambrian Research* **131**, 231–82.

Griffin WL, Wang X, Jackson SE, Pearson NJ, O'Reilly SY, Xu XS and Zhou XM (2002) Zircon chemistry and magma mixing, SE China: in-situ analysis of Hf isotopes, Tonglu and Pingtan igneous complexes. *Lithos* **61**, 237–69.

Gruau G, Bernard-Griffiths J and Lecuyer C (1998) The origin of U-shaped rare earth patterns in ophiolite peridotites: assessing the role of secondary alteration and melt/rock reaction. *Geochimica et Cosmochimica Acta* **62**, 3545–60.

Hawkesworth CJ, Turner SP, McDermott F, Peate DW and Calsteren PV (1997) U–Th isotopes in arc magmas: implications for element transfer from the subducted crust. *Science* **276**, 551–5.

Hu X, Xu CS and Niu SY (1990) *Evolution of the Early Paleozoic Continental Margin in Northern Margin of the North China Platform*. Beijing: Peking University Press, 215 pp. (in Chinese with English abstract).

Huang S and Frey FA (2003) Trace element abundances of Mauna Kea basalt from phase 2 of the Hawaii Scientific Drilling Project: petrogenetic implications of correlations with major element content and isotopic ratios. *Geochemistry, Geophysics, Geosystems* **4**, 1–43.

Jahn BM (2004) The Central Asian Orogenic Belt and growth of the continental crust in the Phanerozoic. In *Aspects of the Tectonic Evolution of China* (eds J Malpas, CJN Fletcher, JR Ali and JC Aitchison), pp. 73–100. Geological Society of London, Special Publications no. 226.

Ji ZJ, Zhang ZC, Chen Y, Li K, Yang JF and Qian XY (2018) Geochemistry, geochronology, and Sr–Nd isotopic compositions of Permian volcanic rocks in the northern margin of the North China Block: implications for the tectonic setting of the southeastern Central Asian Orogenic Belt. *International Journal of Earth Sciences* **107**, 2143–61.

Jia HY, Bao Y and Zhang YQ (2003) Characteristics and tectonic significance of the Wude suture zone in northern Damaoqi, Inner Mongolia. *Journal of Chengdu University of Technology (Science & Technology Edition)* **30**, 30–4 (in Chinese with English abstract).

Jian P, Liu DY, Kröner A, Windley BF, Shi YR, Zhang FQ, Shi GH, Miao LC, Zhang W, Zhang Q, Zhang LQ and Ren JS (2008) Time scale of an early to mid-Paleozoic orogenic cycle of the long-lived Central Asian Orogenic Belt, Inner Mongolia of China: implications for continental growth. *Lithos* **101**, 233–59.

Jiang JY and Zhu YF (2020) Characterization of the Hegenshan podiform chromitites (Inner Mongolia, China): sub-solidus cooling and hydrothermal alteration. *Ore Geology Reviews* **120**, 103413. doi: 10.1016/j.oregeorev.2020.103413.

Kamenetsky V, Crawford AJ and Meffre S (2001) Factors controlling chemistry of magmatic spinel: an empirical study of associated olivine, Cr-spinel and melt inclusions from primitive rocks. *Journal of Petrology* **42**, 655–71.

Kapsiotis A, Rassios AE, Uysal I, Grieco G, Akmaz RM, Saka S and Bussolesi M (2018) Compositional fingerprints of chromian spinel from the refractory chrome ores of Metalleion, Othris (Greece): implications for metallogeny and deformation of chromitites within a "hot" oceanic fault zone. *Journal of Geochemical Exploration* **185**, 14–32.

Khalil AES, Obeid MA and Azer MK (2014) Serpentinized peridotites at the north part of the Wadi Allaqi District (Egypt): implications for the tectonomagmatic evolution of fore-arc crust. *Acta Geologica Sinica* **88**, 1421–36.

Kieffer B, Arndt NA, Lapierre H, Bastien F, Bosch D, Pecher A, Yirgu G, Ayalew D, Weis D, Jerram DA, Keller F and Meugniot C (2004) Flood and shield basalts from Ethiopia: magmas from the African superswell. *Journal of Petrology* **45**, 793–834.

Kröner A, Kovach V, Belousova E, Hegner E, Armstrong R, Dolgopolova A, Seltmann R, Alexeiev DV, Hoffmann JE, Wong J, Sun M, Cai K, Wang T, Tong Y, Wilde SA, Degtyarev KE and Rytsk E (2014) Reassessment of continental growth during the accretionary history of the Central Asian Orogenic Belt. *Gondwana Research* **25**, 103–25.

Kröner A, Lehmann J, Schulmann K, Demoux A, Lexa O, Tomurhuu D, Stipska P, Liu D and Wingate M (2010) Lithostratigraphic and geochronological constrains on the evolution of the Central Asian orogenic belt in SW Mongolia: early Paleozoic rifting followed by Late Paleozoic accretion. *American Journal of Science* **310**, 523–74.

Li X, Zhang L, Wei C, Slabunov AI and Bader T (2018) Quartz and orthopyroxene exsolution lamellae in clinopyroxene and the metamorphic *P–T* path of Belomorian eclogites. *Journal of Metamorphic Geology* **36**, 1–22.

Li WB, Zhong RC, Xu C, Song B and Qu WJ (2012) U–Pb and Re–Os geochronology of the Bainaimiao Cu–Mo–Au deposit, on the northern margin of the North China Craton, Central Asia Orogenic Belt: implications for ore genesis and geodynamic setting. *Ore Geology Reviews* **48**, 139–50.

Li HY, Zhou ZG, Li PJ, Zhang D, Liu CF, Zhao XQ, Chen LZ, Gu CN, Lin TT and Hu MM (2016) Ordovician intrusive rocks from the eastern Central Asian Orogenic Belt in Northeast China: chronology and implications for bidirectional subduction of the early Palaeozoic Palaeo-Asian Ocean. *International Geology Review* **58**, 1175–95.

Liu M, Lai S, Zhang D, Zhu R, Qin J, Xiong G and Wang H (2020) Constructing the latest Neoproterozoic to Early Paleozoic multiple crust-mantle interactions in western Bainaimiao arc terrane, southeastern Central Asian Orogenic Belt. *Geoscience Frontiers* **11**, 1727–42.

Liu CF, Liu WC and Zhou ZG (2014) Geochronology, geochemistry and tectonic setting of the Paleozoic–early Mesozoic intrusive in Siziwangqi, Inner Mongolia. *Acta Geologica Sinica* **88**, 992–1002 (in Chinese with English Abstract).

Ludwig KR (2003) *User's Manual for Isoplot 3.0: A Geochronological, Toolkit for Microsoft Excel*. Berkeley Geochronology Center, Special Publication 4, 71 pp.

Ma X, Chen B, Chen JF and Niu XL (2013) Zircon SHRIMP U–Pb age, geochemical, Sr–Nd isotopic and in-situ Hf isotopic data of the late Carboniferous–early Permian plutons in the northern margin of the North China Craton. *Science China Earth Sciences* **56**, 126–44.

Ma X, Chen B, Chen JF and Qu WJ (2014) Petrogenesis and geodynamic significance of the late Palaeozoic Dongwanzi complex, North China Craton: constraints from petrological, geochemical, and Os–Nd–Sr isotopic data. *International Geology Review* **56**, 1521–40.

Ma SX, Wang ZQ, Zhang YL and Sun JX (2019). Bainaimiao arc as an exotic terrane along the northern margin of the North China Craton: evidences from petrography, zircon U–Pb dating, and geochemistry of the Early Devonian deposits. *Tectonics* **38**, 2606–24.

Ma YL, Zhong Y, Furnes H, Zhaxi Q, Pang JH, Liu WL and Xia B (2021) Origin and tectonic implications of boninite dikes in the Shiquanhe ophiolite, western Bangong Suture, Tibet. *Journal of Asian Earth Sciences* **205**, 104594. doi: 10.1016/j.jseaes.2020.104594.

Miao LC, Fan WM, Liu DY, Zhang FQ, Shi YR and Guo F (2008) Geochronology and geochemistry of the Hegenshan ophiolitic complex: implications for late-stage tectonic evolution of the Inner Mongolia–Daxinganling Orogenic Belt, China. *Journal of Asian Earth Sciences* **32**, 348–70.

Parkinson IJ and Pearce JA (1998) Peridotites from the Izu–Bonin–Mariana forearc (ODP Leg 125): evidence for mantle melting and melt–mantle interaction in a supra-subduction zone setting. *Journal of Petrology* **39**, 1577–618.

Pearce JA (1996) A user's guide to basalt discrimination diagrams. In *Trace Element Geochemistry of Volcanic Rocks: Applications for Massive Sulphide Exploration* (ed. DA Wyman), pp. 79–113. Geological Association of Canada, Short Course Notes vol. 12.

Pearce JA (2014) Immobile element fingerprinting of ophiolites. *Elements* **10**, 101–8.

Pearce JA and Norry MJ (1979) Petrogenetic implications of Ti, Zr, Y, and Nb variations in volcanic rocks. *Contributions to Mineralogy and Petrology* **69**, 33–47.

Pearce JA and Robinson PT (2010) The Troodos ophiolitic complex probably formed in a subduction initiation, slab edge setting. *Gondwana Research* **18**, 60–81.

Pearce JA, Thirlwall MF, Ingram G, Murton BJ, Arculus RJ and Van der Laan SR (1992) Isotopic evidence for the origin of boninites and related rocks drilled in the Izu–Bonin (Ogasawara) forearc, Leg 125. In *Proceedings of the Ocean Drilling Program, Scientific Results, vol. 125* (eds P Fryer, JA Pearce, LB Stokking, JR Ali, R Arculus, D Ballotti, MM Burke, G Ciampo, JA Haggerty, RB Haston, D Heling, MA Hobart, T Ishii, LE Johnson, Y Lagabrielle, FW McCoy, H Maekawa, MS Marlow, G Milner, MJ Motti, BJ Murton, SP Phipps, CA Rigsby, KL Saboda, B Stabell, S van der Laan and Y Xu), pp. 237–61. College Station, Texas.

Peccerillo R and Taylor SR (1976) Geochemistry of Eocene calc-alkaline volcanic rocks from the Kastamonu area, northern Turkey. *Contributions to Mineralogy and Petrology* **58**, 63–81.

Plank T and Langmuir CH (1998) The chemical composition of subducting sediment and its consequences for the crust and mantle. *Chemical Geology* **145**, 325–94.

Polat A and Hofmann AW (2003) Alteration and geochemical patterns in the 3.7–3.8 Ga Isua greenstone belt, West Greenland. *Precambrian Research* **126**, 197–218.

Polat A, Hofmann AW and Rosing MT (2002) Boninite-like volcanic rocks in the 3.7–3.8 Ga Isua greenstone belt, West Greenland: geochemical evidence for intraoceanic subduction zone processes in the early Earth. *Chemical Geology* **184**, 231–54.

Roberts S and Neary C (1993) Petrogenesis of ophiolitic chromitite. In *Magmatic Processes and Plate Tectonics* (eds HM Prichard, T Alabaster, NBW Harris and CR Neary), pp. 257–72. Geological Society of London, Special Publication no. 76.

Safonova I (2017) Juvenile versus recycled crust in the Central Asian Orogenic Belt: implications from ocean plate stratigraphy, blueschist belts and intra-oceanic arcs. *Gondwana Research* **47**, 6–27.

Safonova I, Kotlyarov A, Krivonogov S and Xiao WJ (2017) Intra-oceanic arcs of the Paleo-Asian Ocean. *Gondwana Research* **50**, 167–94.

Saunders AD, Storey M, Kent RW and Norry MJ (1992) Consequences of plume-lithosphere interactions. In *Magmatism and the Causes of Continental Break-up* (eds BC Storey, T Alabaster and RJ Pankhurst), pp. 41–60. Geological Society of London, Special Publication no. 68.

Shao JA (1989) Continental crust accretion and tectono-magmatic activity at the northern margin of the Sino-Korean plate. *Journal of Southeast Asian Earth Sciences* **3**, 57–62.

Shao JA (1991) *Crustal Evolution in the Middle Part of the Northern Margin of Sino-Korean Plate*. Beijing: Peking University Press, 65 pp. (in Chinese with English abstract).

Sharma M and Wasserburg GJ (1996) The neodymium isotopic compositions and rare earth patterns in highly depleted ultramafic rocks. *Geochimica et Cosmochimica Acta* **60**, 4537–50.

Smith EI, Sanchez A, Walker JD and Wang K (1999) Geochemistry of mafic magmas in the Hurricane Volcanic field, Utah: implications for small- and large-scale chemical variability of the lithospheric mantle. *The Journal of Geology* **107**, 433–48.

Söderlund U, Patchett PJ, Vervoort JD and Isachsen CE (2004) The ^{176}Lu decay constant determined by Lu–Hf and U–Pb isotope systematics of Precambrian mafic intrusions. *Earth and Planetary Science Letters* **219**, 311–24.

Stern RJ (2002) Subduction zones. *Reviews of Geophysics* **40**, 1–38.

Stern RJ, Johnson PR, Kröner A and Yibas B (2004) Neoproterozoic ophiolites of the Arabian-Nubian Shield. *Developments in Precambrian Geology* **13**, 95–128.

Stern RJ, Reagan M, Ishizuka O, Ohara Y and Whattam S (2012) To understand subduction initiation, study forearc crust; to understand forearc crust, study ophiolites. *Lithosphere* **4**, 469–83.

Sun SS and McDonough WF (1989) Chemical and isotopic systematics of oceanic basalts: implications for mantle composition and processes. In *Magmatism in the Ocean Basins* (eds AD Saunders and MJ Norry), pp. 313–45. Geological Society of London, Special Publication no. 42.

Tamura A and Arai S (2006) Harzburgite–dunite–orthopyroxenite suite as a record of suprasubduction zone setting for the Oman ophiolite mantle. *Lithos* **90**, 43–56.

Tang KD (1992) *Tectonic Evolution and Minerogenetic Regularities of the Fold Belt along the Northern Margins of Sino-Korean Plate*. Beijing: Peking University Press, 164 pp. (in Chinese with English abstract).

Tang KD and Zhang YP (1991) Tectonic evolution of Inner Mongolia. In *Tectonic Evolution of the Southern Margin of the Paleo-Asian Composite Megasuture* (eds XC Xiao and YQ Tang), pp. 30–53. Beijing: Scientific and Technical Publishing House (in Chinese with English abstract).

Tang WH, Zhang ZC, Li JF, Li K, Chen Y and Luo ZW (2014) Late Paleozoic to Jurassic tectonic evolution of the Bogda area (northeast China): evidence from detrital zircon U–Pb geochronology. *Tectonophysics* **626**, 144–56.

Thanh NX, Rajesh VJ, Itaya T, Windley B, Kwon S and Park CS (2012) A Cretaceous forearc ophiolite in the Shyok suture zone, Ladakh, NW India: implications for the tectonic evolution of the Northwest Himalaya. *Lithos* **155**, 81–93.

Winchester JA and Floyd PA (1977) Geochemical discrimination of different magma series and their differentiation products using immobile elements. *Chemical Geology* **20**, 325–43.

Windley BF, Alexeiev D, Xiao WJ, Kröner A and Badarch G (2007) Tectonic models for accretion of the Central Asian Orogenic Belt. *Journal of the Geological Society, London* **164**, 31–47.

Woodhead JD, Hergt JM, Davidson JP and Eggins SM (2001) Hafnium isotope evidence for 'conservative' element mobility during subduction zone processes. *Earth and Planetary Science Letters* **192**, 331–46.

Wu C, Liu CF, Zhu Y, Zhou ZG, Jiang T, Liu WC, Li HY, Wu C and Ye BY (2016) Early Paleozoic magmatic history of central Inner Mongolia, China: implications for the tectonic evolution of the Southeast Central Asian Orogenic Belt. *International Journal of Earth Sciences* **105**, 1307–27.

Xiao WJ, Windley B, Hao J and Zhai MG (2003) Accretion leading to collision and the Permian Solonker suture, Inner Mongolia, China: termination of the Central Asian Orogenic Belt. *Tectonics* **22**, 1069–89.

Xiao WJ, Windley BF, Huang BC, Han CM, Yuan C, Chen HL, Sun M, Sun S and Li JL (2009) End-Permian to mid-Triassic termination of the accretionary processes of the southern Altaids: implications for the geodynamic evolution, Phanerozoic continental growth, and metallogeny of Central Asia. *International Journal of Earth Science* **98**, 1189–287.

Xu B, Charvet J, Chen Y, Zhao P and Shi G (2013) Middle Paleozoic convergent orogenic belts in western Inner Mongolia (China): framework, kinematics, geochronology and implications for tectonic evolution of the Central Asian Orogenic Belt. *Gondwana Research* **23**, 1342–64.

Xu B, Zhao P, Wang Y, Liao W, Luo Z, Bao Q and Zhou Y (2015) The pre-Devonian tectonic framework of Xing'an–Mongolia orogenic belt (XMOB) in North China. *Journal of Asian Earth Sciences* **97**, 183–96.

Zhai MG and Santosh M (2011) The early Precambrian odyssey of the North China Craton: a synoptic overview. *Gondwana Research* **20**, 6–25.

Zhang ZC, Chen Y, Li K, Li JF, Yang JF and Qian XY (2017) Geochronology and geochemistry of Permian bimodal volcanic rocks from central Inner Mongolia, China: implications for the late Palaeozoic tectonic evolution of the south-eastern Central Asian Orogenic Belt. *Journal of Asian Earth Sciences* **135**, 370–89.

Zhang W and Jian P (2008) SHRIMP dating of early Paleozoic Granites from North Damaoqi, Inner Mongolia. *Acta Geologica Sinica* **82**, 778–87 (in Chinese with English abstract).

Zhang ZC, Li K, Li JF, Tang WH, Chen Y and Luo ZW (2015) Geochronology and geochemistry of the Eastern Erenhot ophiolitic complex: implications for the tectonic evolution of the Inner Mongolia–Daxinganling Orogenic Belt. *Journal of Asian Earth Sciences* **97**, 279–93.

Zhang JF, Liu ZH, Guan QB, Xu ZY, Wang XA and Zhu K (2017). Age and geological significance of Xuniwusu Formation from Bainaimiao area of Sonid Youqi, Inner Mongolia. *Acta Petrologica Sinica* **33**, 3147–60 (in Chinese with English abstract).

Zhang YP, Su YZ and Li JC (2010) Regional tectonic significance of the late Silurian Xibiehe Formation in central Inner Mongolia, China. *Geological Bulletin of China* **29**, 1599–605 (in Chinese with English abstract).

Zhang JR, Wei CJ and Chu H (2018) Multiple metamorphic events recorded in the metamorphic terranes in central Inner Mongolia, Northern China:

implication for the tectonic evolution of the Xing'an-Inner Mongolia Orogenic Belt. *Journal of Asian Earth Sciences* **167**, 52–67.

Zhang SH, Zhao Y, Song B, Hu JM, Liu SW and Yang YH (2009) Contrasting Late Carboniferous and late Permian–Middle Triassic intrusive suites from the northern margin of the North China Craton: geochronology, petrogenesis, and tectonic implications. *Geological Society of America Bulletin* **121**, 181–200.

Zhang SH, Zhao Y, Song B and Wu H (2004) The late Paleozoic gneissic granodiorite pluton in early Precambrian high grade metamorphic terrains near Longhua county in northern Hebei province, north China: result from zircon SHRIMP U–Pb dating and its tectonic implications. *Acta Petrologica Sinica* **20**, 621–6 (in Chinese with English abstract).

Zhang SH, Zhao Y, Song B, Yang ZY, Hu JM and Wu H (2007) Carboniferous granitic plutons from the northern margin of the North China Block: implications for a late Palaeozoic active continental margin. *Journal of the Geological Society, London* **164**, 451–63.

Zhang SH, Zhao Y, Ye H, Liu JM and Hu ZC (2014) Origin and evolution of the Bainaimiao arc belt: implications for crustal growth in the southern Central Asian orogenic belt. *Geological Society of America Bulletin* **126**, 1275–300.

Zhao GC, Sun M, Wilde SA and Li SZ (2003) Assembly, accretion and breakup of the Paleo-Mesoproterozoic Columbia supercontinent: records in the North China Craton. *Gondwana Research* **6**, 417–34.

Zhou H, Pei FP, Zhang Y, Zhou ZB, Xu WL, Wang ZW, Cao HH and Yang C (2018a) Origin and tectonic evolution of early Paleozoic arc terranes abutting the northern margin of North China Craton. *International Journal of Earth Sciences* **107**, 1911–33.

Zhou MF, Robinson PT, Malpas J, Edwards SJ and Qi L (2005) REE and PGE geochemical constraints on the formation of dunites in the Luobusa Ophiolite, Southern Tibet. *Journal of Petrology* **46**, 615–39.

Zhou MF, Robinson PT, Su BX, Gao JF, Li J, Yang JS and Malpas J (2014) Compositions of chromite, associated minerals, and parental magmas of podiform chromite deposits: the role of slab contamination of asthenospheric melts in suprasubduction zone environments. *Gondwana Research* **26**, 262–83.

Zhou H, Zhao GC, Han YG and Wang B (2018b) Geochemistry and zircon U–Pb-Hf isotopes of Paleozoic intrusive rocks in the Damao area in Inner Mongolia, northern China: implications for the tectonic evolution of the Bainaimiao arc. *Lithos* **314–15**, 119–39.

https://doi.org/10.1017/S0016756821000662 Published online by Cambridge University Press